Building and Environment 205 (2021) 108175

Contents lists available at ScienceDirect

Building and Environment

journal homepage: www.elsevier.com/locate/buildenv

Validation of a CFD model for the evaluation of urban microclimate at high latitudes: A case study in Trondheim, Norway

Johannes Brozovsky [a,*], Are Simonsen [b], Niki Gaitani [a]

[a] Department of Architecture and Technology, Faculty for Architecture and Design, NTNU – Norwegian University of Science and Technology, 7491, Trondheim, Norway
[b] Process Technology, SINTEF Industry, S.P. Andersens Veg 15B, 7031, Trondheim, Norway

ARTICLE INFO

Keywords:
Urban microclimate
Computational fluid dynamics
Validation study
Cold climate
Materials

ABSTRACT

The urban microclimate is a rapidly evolving field of research gaining increasing interest from public authorities and researchers. However, studies at high-latitude cities are scarce and researchers primarily focus on summerly overheating. This study focuses on the validation process of a CFD model that applies the 3D URANS approach with the realisable k-ε turbulence model at a highly complex urban area in Trondheim, Norway (63.4° N) during autumn. The CFD model features a polyhedral grid of the urban environment, including geometrically explicitly modelled buildings and trees in the area of interest. Furthermore, solar radiation, longwave radiation exchange, heat transfer from the buildings, heat storage in the urban surface, and the thermal effects of evapotranspiration from trees and grass surfaces are considered. The CFD model is validated with experimental results from a network of five mobile and one reference weather stations in the study area, providing hourly-averaged measurements for wind speed, wind direction (only reference weather station) and air temperature for two 48-h periods from September 27–28 and October 19–20. The results show that the CFD model is well able to reproduce the measured conditions at the area of interest with a mean R^2 of 0.60, 0.63, and 0.96 for wind speed, wind direction and air temperature, respectively, at the reference weather station. It will be used in future studies, including the analysis of the impact of urban microclimate on buildings' energy performance, outdoor thermal and pedestrian wind comfort.

1. Introduction

Urban climatology (UC) is a much-discussed field of research, driven by ongoing global urbanisation, population growth and climate change [1,2]. Urban areas account for around 67–76% of global energy use and between 71 and 76% of CO_2 emissions from global final energy use [1]. Considering these significant shares, solutions are urgently needed to reduce the negative impact of cities on the environment while ensuring a healthy and habitable space for humans. UC combines a variety of different disciplines to deepen the knowledge in how to address these issues, such as meteorology, climatology, air pollution science, architecture, building engineering, physics, urban design, biometeorology, social sciences etc. [3]. While at the beginning of UC research, studies involving the thorough analysis of field observations dominated the methodological approaches, numerical studies gained increasing attention, especially during the last two decades [3–5]. There are several advantages arising from the utilisation of computer simulations, like for instance a weather forecasting model, compared to observational approaches. For instance, different scenarios and strategies can be easily investigated and assessed, and the variables of interest are available for every location in the computational domain and not only for a few measurement points.

In UC, the focus lies generally on the lower part of the troposphere (up to about 1 km). In the horizontal extension, cities are typically located near the border between the meteorological micro- (smaller than 2 km) and the mesoscale (from 2 km to 2000 km), see also Fig. 1 [6]. Therefore, UC is mostly influenced by physical processes at both these scales which impact the so-called microclimate (MC). As human activity primarily takes place within these scales, the MC is of significant importance for people's daily lives.

It is well known that urban areas can have significantly different climatic conditions than their rural surroundings [7]. Most commonly, these differences get apparent as an urban heat island (UHI) which refers to the fact that temperatures in cities are usually higher than their surroundings. Oke [8] gives seven main reasons for that:

1. Increased absorption of short-wave radiation,

* Corresponding author.
E-mail address: johannes.brozovsky@ntnu.no (J. Brozovsky).

https://doi.org/10.1016/j.buildenv.2021.108175
Received 3 May 2021; Received in revised form 6 July 2021; Accepted 18 July 2021
Available online 21 July 2021

Abbreviations

AT	Air temperature
BPG	Best practice guidelines
CFD	Computational fluid dynamics
CO_2	Carbon dioxide
CV_{RMSD}	Coefficient of variance of the root mean square deviation
D_{max}	Maximum deviation
DO	Discrete ordinates
H	Humidity
HF	Heat flux
LAD	Leaf area density
LAI	Leaf area index
LiDAR	Light detection and ranging
MC	Microclimate
MRT	Mean radiant temperature
NTNU	Norwegian University of Science and Technology
ORM	Obstacle resolving meteorological models
OSM	On-site measurements
PET	Physiological equivalent temperature
PME	Penman-Monteith equation
R^2	Coefficient of determination
RANS	Reynolds averaged Navier-Stokes
RS	Remote sensing
SET	Standard effective temperature
SOT	Soil temperature
SR	Solar radiation
ST	Surface temperature
SVF	Sky view factor
UC	Urban climate
UDF	User defined function
URANS	Unsteady Reynolds averaged Navier-Stokes
VP	Validation period
WD	Wind direction
WS	Wind speed
WT	Wind tunnel

2. Increased long-wave radiation from the sky,
3. Decreased long-wave radiation loss,
4. Anthropogenic heat sources,
5. Increased sensible heat storage,
6. Decreased evapotranspiration,
7. Decreased total turbulent heat transport.

Especially during heat waves, these causes can negatively impact the urban environment and lead to unfavourable conditions [9,10], excess mortality [11–13] and increased building cooling demands [13–15]. However, in cold climate regions, it was reported that savings from the heating energy demand during winter were larger than increases in cooling energy demand during summer [16,17]. With the expected rise in the frequency of extreme climate events and the advancements of methodological and technical capabilities, the urban MC has therefore been introduced increasingly into the design process of buildings and cities. Many publications stress the necessity of improving the design and the climate resilience of cities and their outdoor environment to provide comfortable spaces that invite people to spend time outdoors or that promote soft mobility, regardless of their climate [18–20].

At the microscale, especially Computational Fluid Dynamics (CFD) has emerged as a method to study different aspects of the MC such as wind flow, heat convection, conductivity and storage, short and long wave radiation exchange, natural convection, water vapour transfer, pollutant/particle dispersion etc. Although mesoscale processes like the Coriolis effect, atmospheric vertical mixing or cloud formation are usually not considered in microscale CFD modelling, the computational cost of transient simulations that cover more physics than just fluid flow is generally very high. Therefore, the size of the computational domain of such studies is typically limited to a couple of blocks within a city that are explicitly modelled, while the larger surroundings are included implicitly, for example with an imposed roughness index [21].

Besides for instance pedestrian wind comfort [22–26], pollutant dispersal [27–30] or wind-driven rain [31–33], CFD has been used extensively to investigate the thermal conditions in real urban areas (see Table 1). Many of these studies focused on topics such as cooling strategies [34–52] or outdoor thermal comfort [53–62]. About half of the studies (51.1%) were conducted with ENVI-Met [63], a three-dimensional non-hydrostatic tool for the surface-plant-air interaction that is increasingly used to evaluate different scenarios like the effect of different greening strategies, surface characteristics and urban morphology on the MC or outdoor thermal comfort. In 77.8% of the studies, the effects of vegetation on the local climatic conditions were considered.

Table 1 also shows that the majority (75.6%) of the listed publications provided a validation process, even though the degree of detail and number of climate variables in the validation varied significantly. The most frequently used climate variable for validation was the air

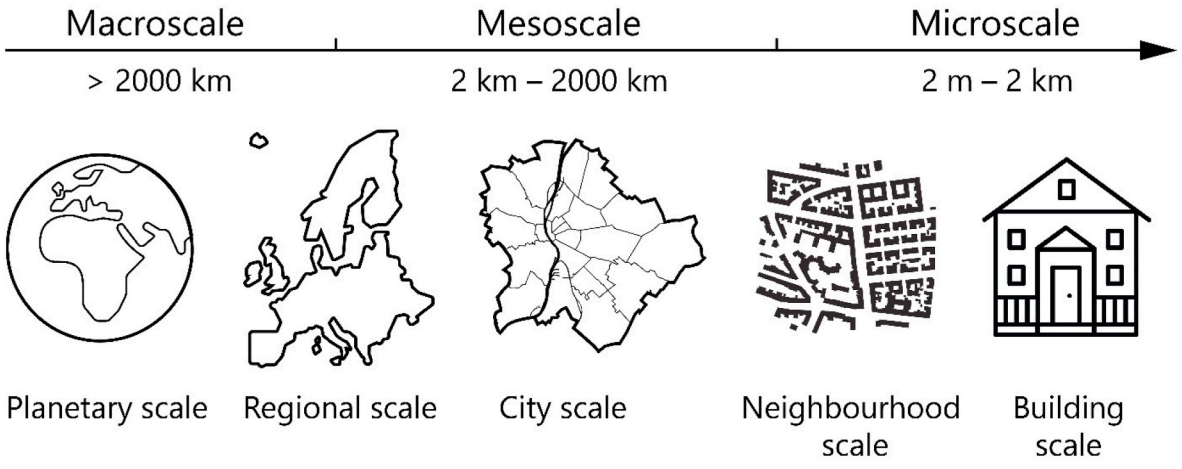

Fig. 1. Terminology of climatological scales with their horizontal extension from Ref. [6].

Table 1
Overview of published articles on the thermal conditions in real urban areas. The column "Validation variables" lists the variables that were compared to experimental data: Air temperature (AT); humidity (H); heat flux (HF); mean radiant temperature (MRT); Physiological Equivalent Temperature (PET); Standard Effective Temperature (SET); soil temperature (SOT); solar radiation (SR); surface temperature (ST); sky view factor (SVF); wind direction (WD); wind speed (WS). The column "Validation data" refers to the data acquisition method: On-site measurements (OSM); wind tunnel (WT); remote sensing (RS).

Authors	Year	Reference	City, country	Research focus	Validation variables	Validation data	Vegetation considered	ENVI-Met
Chen et al.	2004	[53]	Shenzhen, China	Pedestrian level comfort at an apartment block	AT, ST, WS, H, MRT, SET	OSM	Yes	No
Takahashi et al.	2004	[72]	Kyoto, Japan	Measurement and CFD prediction of the thermal environment	AT, HF	OSM	Yes	No
Huang et al.	2005	[59]	Tokyo, Japan	Simulation and measurement of urban thermal environment	AT, WS, H	OSM	No	No
Priyadarsini et al.	2008	[66]	Singapore	Key factors of the UHI	AT, WS	OSM, WT	No	No
Chen et al.	2009	[34]	Tokyo, Japan	Different mitigation scenarios for the UHI	–	–	Yes	No
Hsieh et al.	2010	[35]	Tokyo, Japan	Site design and layout planning to mitigate the thermal environment	–	–	Yes	No
Chow et al.	2011	[73]	Tempe, AZ, USA	Horizontal and vertical nocturnal cooling influence of a small park	AT	OSM	Yes	Yes
Fintikakis et al.	2011	[48]	Tirana, Albania	Improving the urban microclimatic and thermal comfort conditions	AT, ST, WS, WD	OSM	Yes	No
Gaitani et al.	2011	[49]	Athens, Greece	Improve thermal comfort conditions in open spaces	AT, ST, WS, WD	OSM	Yes	No
Kaoru et al.	2011	[74]	Osaka, Japan	Solar and longwave radiation model to simulate air flow and temperature	–	–	No	No
Synnefa et al.	2011	[52]	Athens, Greece	UHI mitigation potential of cool asphalt	–	–	No	No
Chow et al.	2012	[36]	Phoenix, AZ, USA	Xerophytic trees in residential yards as UHI mitigation approach	AT	OSM	Yes	Yes
Ma et al.	2012	[54]	Beijing, China	Method to predict outdoor thermal environment in a residential district	AT, WS	OSM	Yes	No
Santamouris et al.	2012	[51]	Athens, Greece	Design of a rehabilitation plan for an urban area to improve the microclimate	AT, ST, WS, WD	OSM	Yes	No
Santamouris et al.	2012	[50]	Athens, Greece	Using cool pavements to improve the urban microclimate	AT, ST	OSM	Not indicated	No
Shahidan et al.	2012	[37]	Putrajaya, Malaysia	Impact of materials and trees on mitigating the UHI and reducing building cooling demands	AT, ST	OSM	Yes	Yes
Carnielo and Zinzi	2013	[38]	Rome, Italy	Effect of cool materials on the microclimate of an urban neighbourhood	ST	OSM	Yes	Yes
Srivanit et al.	2013	[39]	Saga, Japan	Cooling effect of different greening strategies at a university campus	AT, H, WS, SR	OSM	Yes	Yes
Yang et al.	2013	[75]	Guangzhou, China	Evaluation of a microclimate model to predict the thermal behaviour of surfaces	AT, ST, HF, H, SOT	OSM	Yes	Yes
Maragkogiannis et al.	2014	[76]	Chania, Greece	Terrestrial laser scanning and CFD to study urban thermal environment	–	–	No	No
Su et al.	2014	[40]	Nanjing, China	Impact of greenspace patterns on land surface temperature	ST	OSM	Yes	Yes
Taleghani et al.	2014	[41]	Portland, OR, USA	Courtyard vegetation, ponds, and high albedo surfaces as UHI mitigation strategies	AT	OSM	Yes	Yes
Salata et al.	2015	[62]	Rome, Italy	Impact of material albedo and vegetation on urban microclimate	AT, MRT, H, SR	OSM	Yes	Yes
Targhi and Van Dessel	2015	[55]	Worcester, MA, USA	Influence of urban geometry on outdoor thermal comfort conditions	–	–	Yes	Yes
Tominaga et al.	2015	[42]	Hadano, Japan	Evaporative cooling effect from water bodies	AT, H	OSM	No	No
Toparlar et al.	2015	[65]	Rotterdam, Netherlands	Validation of a CFD simulation model of urban microclimate	ST	RS	No	No
Wang and Akbari	2015	[43]	Montreal, Canada	Different UHI mitigation strategies	AT	OSM	Yes	Yes
Berardi	2016	[44]	Toronto, Canada	Energy savings and outdoor microclimate benefits from green roof retrofits	SVF, AT	OSM	Yes	Yes
Berardi and Wang	2016	[77]	Toronto, Canada	Microclimatic effect of city densification	AT	OSM	Yes	Yes
Kim et al.	2016	[45]	Seoul, Korea	Cooling effect of different land cover on surface and air temperatures	ST	OSM	Yes	Yes
Lee et al.	2016	[60]	Freiburg, Germany	Reduce human heat stress through trees and grasslands	AT, MRT, PET	OSM	Yes	Yes
Quaid et al.	2016	[61]	Putrajaya, Malaysia	UHI and thermal comfort conditions	AT	OSM	Yes	Yes
Wang et al.	2016	[46]	Toronto, Canada	Different UHI mitigation strategies	AT	OSM	Yes	Yes
Allegrini and Carmeliet	2017	[78]	Zürich, Switzerland	Effect of new buildings on the local urban microclimate	–	–	No	No
Park et al.	2017	[79]	Jeonju, Korea	Microclimate of urban infrastructure regeneration programs	–	–	Yes	No
Karakounos et al.	2018	[56]	Serres, Greece	Different scenarios for improving outdoor thermal comfort	–	–	Yes	Yes
Kyrakodis and Santamouris	2018	[47]	Athens, Greece	Mitigation of the UHI using reflective pavements	AT, ST	OSM	Yes	Yes

(continued on next page)

Table 1 (*continued*)

Authors	Year	Reference	City, country	Research focus	Validation variables	Validation data	Vegetation considered	ENVI-Met
Taleghani and Berardi	2018	[57]	Toronto, Canada	Effect of pavement characteristics on outdoor thermal comfort	–	–	Yes	Yes
Toparlar et al.	2018	[80]	Antwerp, Belgium	Effect of an urban park on microclimate in its vicinity	AT	OSM	Yes	No
Toparlar et al.	2018	[81]	Antwerp, Belgium	Impact of urban microclimate on summertime building cooling demand	AT	OSM	Yes	No
Antoniou et al.	2019	[71]	Nicosia, Cyprus	Validation of a CFD simulation model of urban microclimate	AT, ST, WS	OSM	No	No
Brozovsky et al.	2019	[82]	Trondheim, Norway	Microclimatic conditions at a university campus	ST	OSM	Yes	Yes
Ghaffarianhoseini et al.	2019	[58]	Kuala Lumpur, Malaysia	Thermal comfort conditions at a university campus	AT	OSM	Yes	Yes
Yang and Li	2020	[83]	Xiantao, China	Urban thermal environment of an urban area within a network of water channels	–	–	Yes	No
Brozovsky et al.	2021	[64]	Trondheim, Norway	Influence of different design strategies and the urban fabric on outdoor thermal comfort conditions	AT, ST, H, WS, WD	OSM	Yes	Yes
This study	–	–	Trondheim, Norway	Validation of a CFD model for urban microclimate evaluation	AT, WS, WD	OSM	Yes	No

temperature (85.3% of validation studies). Surprisingly, only few studies validated wind speed (29.4% of validation studies) while wind direction has been validated only in four (11.8 %) studies [48,49,51,64]. However, in three of these publications [48,49,51], only the wind direction patterns were compared, and no quantitative analysis of accordance was presented. In all except for one publication by Toparlar et al. [65] where remote sensing (RS) was used to get surface temperatures from satellite imagery, on-site measurements (OSM) provided the validation data. In one case, wind tunnel measurements were carried out to obtain validation data in addition to OSM [66].

Most commonly, CFD MC studies were carried out for locations in temperate and warm climate zones during summer conditions, while there is a clear lack of urban MC studies in climatic regions close to or above the Arctic Circle, as pointed out e.g. in a review by Toparlar et al. [4] or in a research paper by Ebrahimabadi et al. [67]. Considering that more than 25 million people live above 60° N, UC and MC research in the cold-climate and high-latitude regions of the world can contribute to resilient and sustainable urban (re)development and improve the living quality of many. Additionally, a large number of cities in temperate climate experience pronounced cold periods for significant parts of the year and would benefit from research in cold climate non-summer conditions.

Numerical models are often used without sufficient proof of their accuracy. In fact, validation is an essential part of applying a numerical model and is defined as the process of determining how well simulations represent the real world by using physical observations as a reference [68]. Moreover, in practice, the quality of the results are not only dependent on the capabilities of the used software, but to a considerable degree also on the input of the user, as human errors cannot be eliminated entirely [69]. It is therefore indispensable to ensure that a numerical model meets the requirements specified for its planned purpose [68,70].

Similar to previous studies [65,71], this article presents the validation of a CFD model to investigate the urban MC in the software ANSYS Fluent 2020.R1 by using field measurements. Unlike the vast majority of published articles (as indicated in Table 1), this work addresses the MC at an urban high-latitude and cold-climate location at the campus of the Norwegian University of Science and Technology (NTNU) in Trondheim, Norway. The aim of this study is to investigate the applicability of a CFD model for the analysis of the MC in a complex, high-latitude urban setting during autumn. In this article, the inclusion of the Penman-Monteith equation (PME) to account for evapotranspirational cooling from grass-covered surfaces is described. Furthermore, the outdoor thermal comfort index Physiological Equivalent Temperature (PET) has been implemented in the CFD model. To the best of our knowledge, neither the PME nor the PET has been implemented in ANSYS Fluent in a previously published article for studying the urban MC. The range of applications for CFD models such as the one in this study are many as it can be used not only for evaluating the thermal environment, like studying the outdoor thermal comfort or the influence of MC on building energy demand, but also to evaluate the local wind conditions for urban wind energy generation, pollutant dispersion, or determining pressure coefficients for natural ventilation potential.

In section 2, the study area, on-site measurements, computational settings, structure and grid of the CFD model are described. Section 3 presents the results of a grid-convergence analysis and the validation of the CFD model for two 48-h periods in autumn 2019. The paper concludes with section 4 (discussion) and 5 (conclusions).

2. Methodology

2.1. Study area and local climate

This study was carried out at the NTNU campus in Trondheim, Norway. The city lies at a latitude of 63.4° N, has 200,000 inhabitants, and is located at the coast of a large fjord. NTNU's campus *(Gløshaugen)* is approximately 0.26 km^2 in size and is situated ca. 1.5 km south of the city centre at an altitude between 38 and 49 m a.s.l. Trondheim is embedded in complex terrain and mainly characterized by a mix of dense, but low-rise built-up and open, park-like areas, frequently traversed by patches of forests (see Fig. 2).

The Köppen-Geiger climate type for Trondheim is oceanic (Dfb), but closely borders continental, subpolar and subarctic climates [85]. From November to March, moderate snowfall with periods of milder weather patterns and rain are common. With 4.8 °C (1961–1990), the annual mean temperature is quite cool, including relatively short and mild summers, and long and cool winters. Due to climate change, temperatures in the arctic and subarctic regions have been rising over the last decades. In Trondheim, the mean annual temperature from 1991 to 2020 was 1.0 °C higher (5.8 °C) than in the norm period from 1961 to 1990 [86].

Due to the significant warming effect of the Gulf Stream, Norway's coastal cities have a rather mild climate considering their comparatively high latitudes [87]. Thus, even though Trondheim and Toronto, Canada, being classified by the same Köppen-Geiger climate type, from a UC point of view, they cannot be treated climatologically as equivalent. Not only are the two cities different in terms of their size, topography, morphology etc., but also with regard to the availability of solar radiation. The access to which is considered to be key to human outdoor thermal comfort [88–91] and to reduce building energy demands [92]

Fig. 2. (a) Location of Trondheim within Norway and Fennoscandia. (b) Aerial photograph of Trondheim's built-up area (from the Norwegian Mapping Authority, www.kartverket.no). (c) Surrounding of the NTNU campus with aerodynamic roughness length z_0 indicated according to the updated Davenport roughness classification [84] (data from the Norwegian Mapping Authority). (d) Site plan of the NTNU campus with indication of geometrical building modelling degree, surface types, and location of mobile and reference weather stations.

(e.g. passive solar gains, solar thermal or photovoltaics production). These differences in solar access are caused by the location of the two cities in terms of latitude (see Table 2). The almost 20° lower sun elevation angles in Trondheim, together with complex, mountainous terrain and an urban landscape result in high shading levels and short days during the cold season. Therefore, at this particular time of the year, low sun angles need to be taken into consideration in high-latitude cities as they can be detrimental to sustainable urban development.

2.2. Measurement campaign

In order to capture the microclimatic conditions on-site, a mea-

Table 2
Sun elevation angles for different dates in Toronto, Canada and Trondheim, Norway.

Date	Max. sun elevation angle	
	Toronto, Canada (43.6° N)	Trondheim, Norway (63.4° N)
21.03. (vernal equinox)	47.0°	27.1°
21.06. (summer solstice)	69.8°	50.0°
23.09. (autumnal equinox)	45.9°	26.2°
21.12. (winter solstice)	22.9°	3.3°

surement campaign was conducted from September 23 to October 21, 2019. Fig. 2 shows the fixed location of five mobile weather stations (see also Fig. 3) that recorded air temperature ($T_{a,C}$) [°C], relative humidity (*RH*) [%], wind speed (*WS*) [m s^{-1}] and direction (*WD*) [°] in 0.1 Hz intervals in a height of 3 m. A fixed weather station, 10 m above the roof of the VATL building (28 m above the ground) is used as a reference station for calibration. At the reference weather station, also global horizontal radiation (S_g) was measured. The recorded climate variables from the reference weather station served as a basis for the input at the domain boundaries in the simulations. Fig. 4 shows the data flow of the climate variables in this study. The accuracies of the sensors are listed in Table 3.

For validation purposes, two distinct 48-h validation periods (VP) during the measurement campaign are selected that contain at least one very sunny day, relatively strong fluctuations and a relatively high average of wind speed, a pronounced diurnal temperature variation and preferably a large variation of wind direction. These criteria are established to verify the CFD model's performance under demanding and large variety of conditions. The selected days are September 27–28 (VP1) and October 19–20 (VP2). During both periods, a pronounced variability in wind speed occurred at the reference weather station, ranging between 1.2 and 4.5 m s^{-1} in VP1 and between 0.7 and 4.2 m s^{-1} in VP2. In VP2 strong fluctuations in wind direction were observed, while VP1 contained only minor changes in wind direction (south-east to south-west). The air temperature ranged from 9.0 to 16.9 °C in VP1 and 3.6–8.5 °C in VP2. The hourly global horizontal radiation reached 400 W m^{-2} in VP1 and 200 W m^{-2} in VP2. Graphs of the climate variables used for validation during both VPs are presented in the results section.

2.3. Computational domain

The computational domain of the study area features regions of three different types of geometrical modelling: (a) where buildings and trees are represented explicitly with a rather high degree of details (NTNU

Fig. 3. Weather station B on a lawn behind the main building (HB) in mid-October 2019.

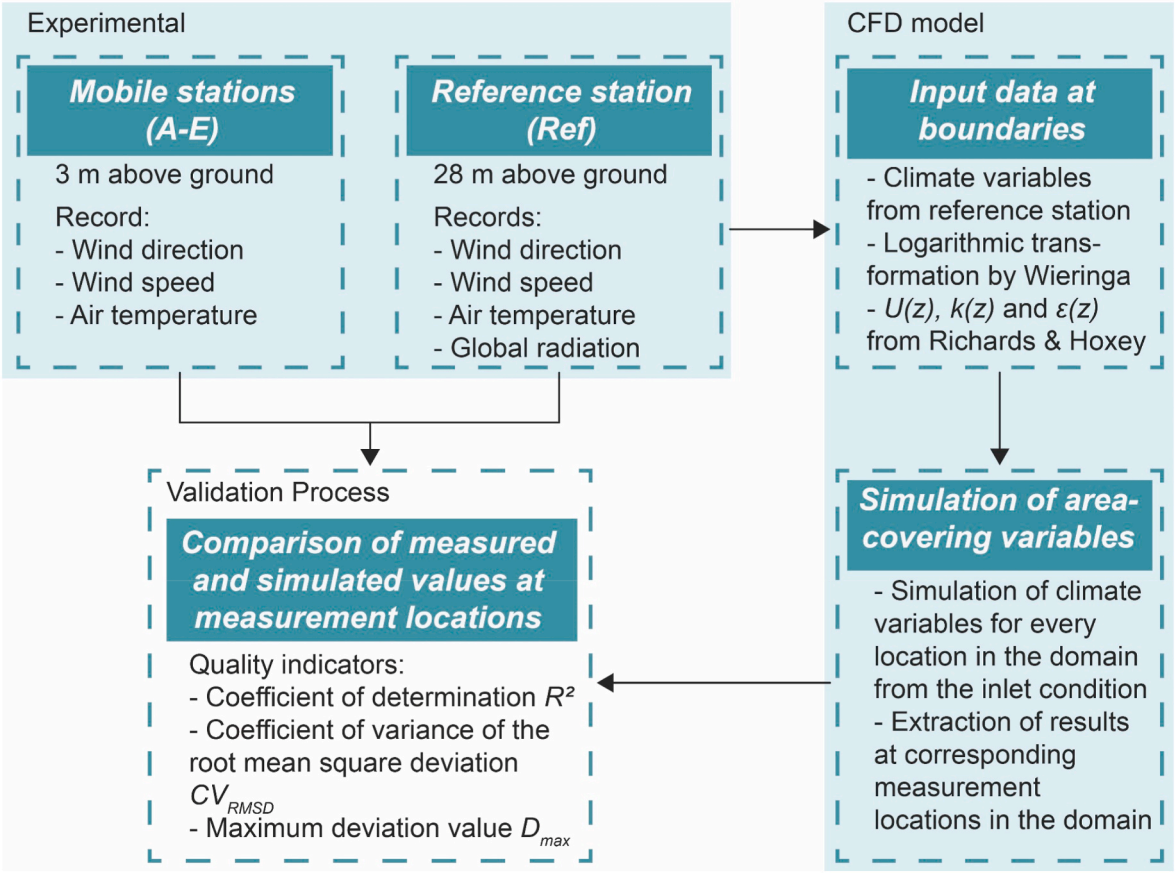

Fig. 4. Schematic illustration of the data flow of climate variables in this study.

Table 3
Accuracy of the sensors mounted on the mobile and the reference weather stations.

Weather station	*WD*	*WS*	$T_{a,C}$	S_g
Mobile stations	±5° at 1.4° resolution	±1.1 m s^{-1} or ±4% of reading at 0.5 m s^{-1} resolution	±0.21 °C from 0 °C to 50 °C	–
Reference station	±2° RMSE at 0.1° resolution	±0.2 m s^{-1} or ±2% of reading at 0.01 m s^{-1} resolution	±0.15 °C or ±0.1% of reading	2nd class pyranometer at 1 W m^{-2} resolution

campus), (b) the area around the NTNU campus, where only buildings and no vegetation are represented explicitly yet with a lower degree of details (representation of buildings as simple boxes), and (c) the wider area surroundings of (a) and (b) which are only represented implicitly by assigning an aerodynamic roughness length z_0 according to the Davenport-Wieringa roughness classification [84].

There are two main sources of geometrical data in this study. (1) A freely available 3D geometrical city model from Trondheim Municipality and (2) Light detection and ranging (LiDAR) data created at NTNU. The data from Trondheim Municipality contains detailed geometrical information of the terrain and the position of buildings at the location of the computational domain. However, it does not contain elements like street signs, bus stops, lamp posts, curbs, vehicles, statues or small monuments and public artwork. Furthermore, the building geometries are not watertight and often show a deficient geometrical representation of complex roof shapes for instance. Thus, the buildings surrounding NTNU campus (see Figs. 2 and 5) were simplified into box-like geometries, omitting details like balconies, protrusions, oriels etc. These simplifications conserved the footprint but changed the height of the building which was taken as the mean height of the building's eaves and ridge for pitched roofs. Furthermore, smaller elements like garden sheds, dog houses etc. were omitted. Rhino 5 was used for these modifications.

The LiDAR-based data provides higher accuracy and geometrical quality of the building on campus and was provided in form of a Trimble SketchUp file. Nevertheless, most of the buildings were geometrically remodelled as also the LiDAR data exhibited some geometrical deficiencies such as distorted faces, holes etc. Three newer buildings (ZEB, TCL and LL, see Fig. 5) on campus that are not included in this data were then designed in Trimble SketchUp according to their technical drawings.

Both, the Rhino file containing the modified data from Trondheim Municipality and the SketchUp file of the campus buildings were imported into ANSYS SpaceClaim 2020.R1 and merged. In SpaceClaim, the dimensioning of the domain, positioning of the tree geometries according to on-site visits and satellite images was performed.

Satisfying the suggestion from the CFD best practice guidelines (BPG) by Franke et al. [93] and Tominaga et al. [94], all buildings within a distance of at least 250 m (at least one street block) around the campus buildings are included to act as a direct obstacle to the wind flow. The height of the highest building in the area of interest (on the campus) is 44.5 m, the highest geometrically explicitly modelled building is 73 m and is located about 300 m south-west of the campus. The surrounding terrain is quite complex and ranges in elevation from 0 to 172 m a.s.l., causing obstructions to the wind flow much higher than the modelled buildings. Therefore, the domain's bottom boundary was copied to the top, so that they largely have the same shape (the only difference is the lower grid resolution at the top) and all lateral

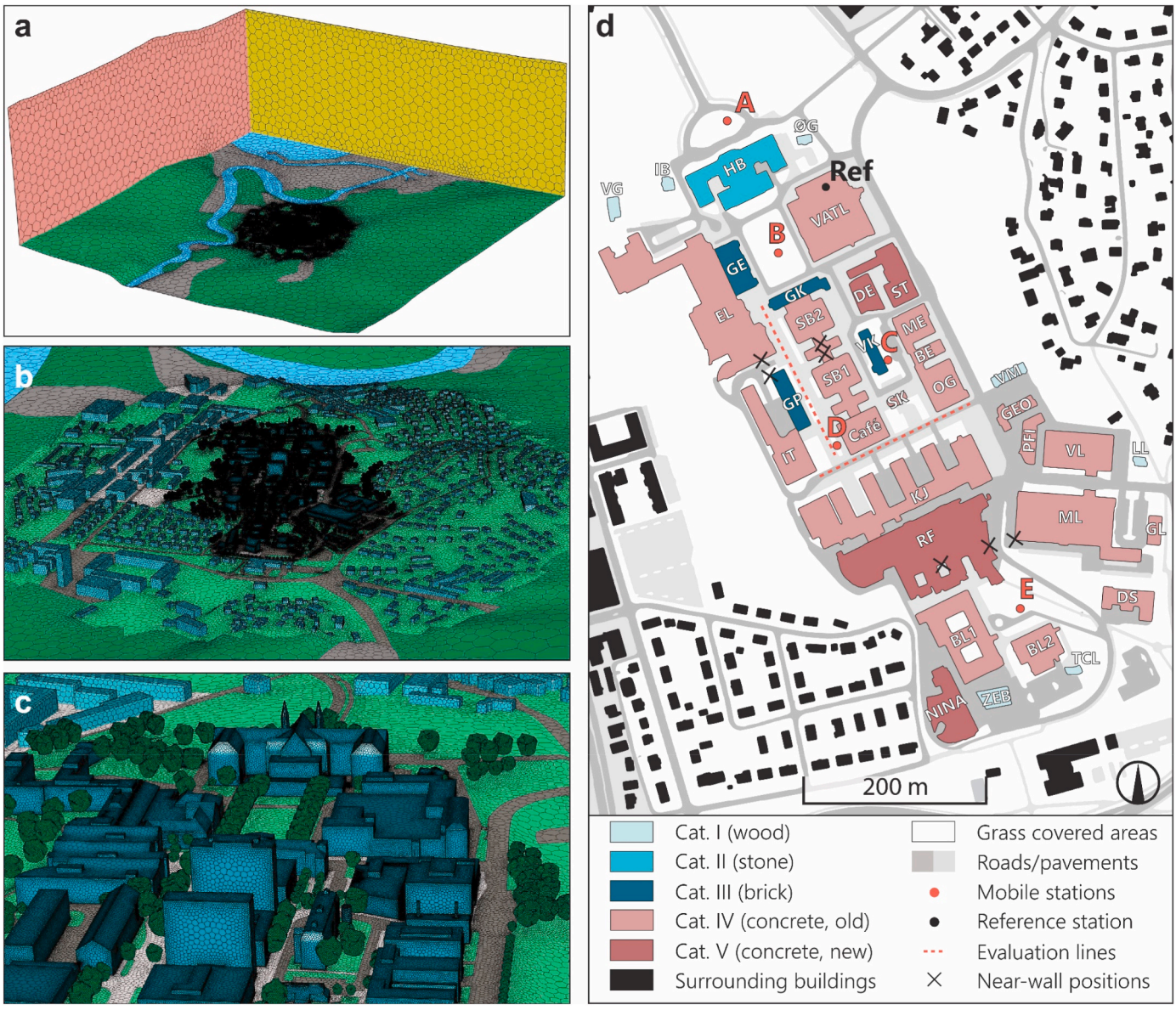

Fig. 5. Computational domain (4225 × 4225 × 1550 m^3) with 9,123,834 cells; (a) View from south-east with different surface types: water (blue), primarily green spaces (green), densely built-up or industrial areas (grey), northern (yellow) and western (red) boundary; (b) View of the geometrically explicitly modelled area with different surface types: asphalt (dark grey), concrete/pavement (light grey) and green spaces (green); (c) Close-up view of the NTNU campus buildings and trees; (d) Building categories, surface types, positions of the mobile and reference weather stations, the evaluation lines, and near-wall positions for the grid-convergence analysis. (For interpretation of the references to colour in this figure legend, the reader is referred to the Web version of this article.)

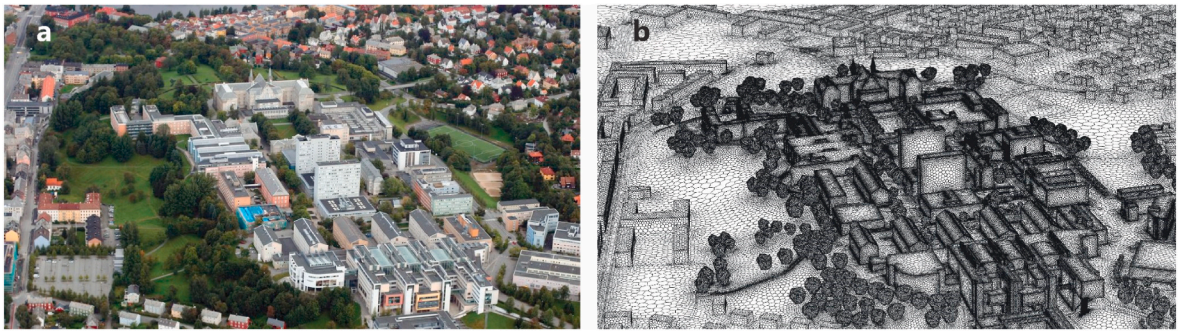

Fig. 6. (a) Aerial view of the NTNU campus from south (photo: Lars Strømmen); (b) Computational grid with 9,123,834 cells, featuring buildings and trees on the campus.

boundaries have the same surface area (see Fig. 5). This way, instead of having a flat top boundary surface, the terrain leads to less constriction in the domain. Only relying on the BPG which do not consider complex terrain would have led to a much smaller domain and a too high blockage ratio. Due to the hourly changing wind direction, always two of the lateral boundaries are set as inlets and two as outlets at a time. The maximum blockage ratio of all buildings and trees is 1.1% which satisfies the BPG [93,94] to keep the blockage ratio below 3%. The resulting domain size is 4225 × 4225 × 1550 m^3.

The domain is discretised into a poly-hexcore grid that consists of 9,123,834 cells (see Fig. 6) with ANSYS Fluent 2020.R1 in meshing mode. The grid is based on a grid-convergence analysis where three meshes of different resolutions were checked for their impact on the solution. For that, wind speed ratios at different locations in the area of interest were compared for a coarse grid with 4,371,409 cells, a basic grid with 9,123,834 cells, and a fine grid with 23, 566, 616 cells. These locations include the five mobile weather stations, the reference weather station, two horizontal lines at 3 m height, and selected near-wall positions as illustrated in Fig. 5. The main difference between the three grids was the sizing of the surface mesh in the area of interest, mainly consisting of the geometrically explicitly modelled buildings and trees (see Table 4). The grid sizing settings near the top and lateral boundaries of the domain were kept the same in the three grids. For all grids, the simulations are carried out using steady-state Reynolds Averaged Navier Stokes (RANS), using the same inlet conditions as described in section 2.3, but with a constant southern wind direction and wind speed of 3 m s^{-1} at 28 m height (the reference weather station). All three grids were created following the BPG [93,94].

In the ultimately selected basic grid, a cell expansion rate of 1.2 ensures a smooth transition of cell sizes between a fine resolution in the area of interest to a coarse mesh in the regions further away. The smallest resulting cell in the domain has a volume of 8.8 cm^3 whereas the largest has 2.3 × 10^6 m^3. As recommended in the BPG [93,94], at least 10 cells are kept between buildings and the evaluation height (1.75 m in this case, as the climate variables at the pedestrian level are of interest) coincides with at least the third cell above ground in the area of interest. Furthermore, inflation layers ensure vertical grid lines on the building walls and the ground surface in the study area.

2.4. Boundary conditions

In order to account for surface roughness elements in the areas of the domain where buildings and other obstacles have not been modelled explicitly, surface roughness parameters are used. Fluent does not allow for the direct input of the aerodynamic roughness length z_0 as given by Wieringa [84], but requires a sand-grain roughness height k_s. For that, the correlation $k_s = 9.793\, z_0\, C_s^{-1}$, where C_s is a roughness constant [−] was used [95]. In Fluent 2020.R1, C_s is limited to a range between 0 and 1. In this study, the default value of 0.5 was kept for all surface types. Asphalt, concrete and pavement surfaces for the geometrical modelling types *a* and *b* were assigned a sand-grain roughness height $k_s = 0.05$ m, while for grass and building surfaces, k_s was set to 0.1 m to account for irregularities and protrusions. Table 5 shows the surface roughness parameters for all rough walls in the domain. For the geometrically explicitly modelled surfaces, the sand-grain roughness was entered directly. Only for the geometrically implicitly modelled surfaces, a conversion from z_0 to k_s was made. Note that the surface roughness of the geometrically implicitly modelled parts of the domain was not calculated but based on the authors' estimations. Fluid-wall interactions are treated with the standard wall functions by Launder and Spalding [96].

To account for the influence of thermal mass, the urban surface and all buildings are modelled according to their construction type, using shell conduction in Fluent. For that, the buildings at the campus are grouped into five categories, see Fig. 5 and Table 6. For simplification, it was not distinguished between the wall and the roof structures. I.e. the constructions listed in Table 6 are used for both, walls and roofs. Windows, doors, balconies and small chimneys were omitted. All geometrically explicitly modelled buildings are assigned a constant indoor temperature of 21 °C. For the surrounding buildings, 0.3 m brick is used for the wall and roof construction. The ground surface has a thickness of 10 m and a constant temperature of 5 °C at the exterior surface (not facing the fluid cells). This temperature boundary condition is based on groundwater temperature measurements near the study site. The water-covered areas, namely the river Nidelva and Trondheim Fjord are not modelled as a fluid but as a "thin wall" with temperatures recorded at ships traversing the Norwegian coastline and Trondheim Fjord at the simulated dates [97]. The temperatures used as boundary conditions were 15 °C in VP1 and 9 °C in VP2. The grass surfaces are divided into three layers of earth with a top layer thickness of only 0.01 m as there, the evapotranspirational cooling flux from the grass is applied (see section 2.5). As this heat flux is applied in the centre of the respective layer, a thickness of 0.01 m ensures this cooling flux is close to the surface facing the fluid cells. Table 7 lists the optical and thermal properties of the surface materials that were used in the model.

For the simulation, it is specified that always two of the lateral domain boundaries are set as inlets and the other two as outlets, depending on the wind direction. At the inlets, a logarithmic profile of the air velocity $U(z)$ [m s^{-1}] (see Eq. (1)) is imposed. Depending on the wind direction, different surface roughness lengths $z_{0,b}$ [m] at the inlet boundaries are used to determine the shape of the profile. Due to the coastal location of Trondheim, the northern boundary is bordering the sea, for which a different $z_{0,b}$ was used than for the other three boundaries that are located on land (see Fig. 2). Therefore, it is estimated that $z_{0,\,b} = 0.25$ m, based on the terrain, farmland, patches of forests and the built-up areas upwind of the study area between 65 and 310° from north. For the remaining directions, $z_{0,\,b}$ is set to a lower value of 0.1 m. Although, according to the surface type categories from Wieringa [84] a roughness length of 0.002 m should be chosen for the ocean, it was

Table 4
Surface grid sizing settings of the three investigated computational grids in the grid-convergence analysis.

	Element in domain	Coarse grid (4.4 M cells)	Basic grid (9.1 M cells)	Fine grid (23.6 M cells)
Node distance at edges [m]	Cat. I	0.35	0.25	0.2
	Cat II–V	1.0	0.75	0.6
	Trees	0.8	0.6	0.45
Max. node distance [m]	Cat. I	2.5	2.0	1.6
	Cat II–V	5.0	4.0	3.2
	Trees	0.8	0.6	0.45
Expansion rate [−]		1.3	1.2	1.1
Number of prism layers [−]	Buildings	2	3	4
	Ground	2	3	4
Thickness of 1st prism layer [m]	Buildings	0.4	0.15	0.1
	Ground	0.6	0.4	0.3
Min. number of cells between buildings		10	10	10

Table 5
Surface roughness settings in the computational domain.

Modelling type	Surface	z_0 [m]	k_s [m]	C_s [−]
Explicit	Building surfaces	–	0.10	0.5
	Asphalt	–	0.05	0.5
	Concrete	–	0.05	0.5
	Grass-covered earth	–	0.10	0.5
Implicit	Urban cityscape	1.0	19.59	0.5
	Industry	1.0	19.59	0.5
	Other[a]	0.5	9.79	0.5

[a] Combining the surface types *Dense low-rise*, *Farmland*, *Open area*, and *Forest* (see Fig. 2) into one boundary condition type.

Table 6
Wall structure of buildings and the urban surface.

Building categories/ Urban surface	Layer 1 (adjacent to fluid cells)		Layer 2		Layer 3 (domain's exterior)	
	Material	d [m]	Material	d [m]	Material	d [m]
I (Wood)	Wood: spruce	0.05	Insulation	0.25	Wood: spruce	0.05
II (Stone)	Granite	0.2	Brick	0.2	–	–
III (Brick)	Brick	0.36	–	–	–	–
IV (Concrete, old)	Concrete	0.36	–	–	–	–
V (Concrete, new)	Plaster	0.02	Insulation	0.2	Concrete	0.2
Surrounding buildings	Brick	0.3	–	–	–	–
Roads	Asphalt	0.3	Granite	1.0	Earth	8.7
Pavement	Concrete	0.3	Granite	1.0	Earth	8.7
Grass	Earth	0.01	Earth	0.49	Earth	9.5

Table 7
Selected optical and thermal properties of the surface materials on campus [18, 98–100].

Surface	α [−]	ε [−]	c [kJ kg^{-1} K^{-1}]	δ [kg m^{-3}]	λ [W m^{-1} K^{-1}]
Wood: spruce	0.75	0.90	2310	700	0.17
Asphalt	0.70	0.95	800	2400	0.75
Concrete	0.66	0.95	1000	2300	1.60
Plaster	0.66	0.95	1000	1800	1.00
Insulation (not a surface material)	–	–	840	50	0.05
Granite	0.70	0.95	790	2800	3.00
Earth (covered with grass)	0.77	0.95	1000	1400	1.80
Brick	0.66	0.95	900	2050	0.80

Absorptivity (α), emissivity (ε), heat capacity (c), density (δ), thermal conductivity (λ).

found that $z_{0,b} = 0.1$ m results in a better fit of simulations and measurements which can be partially attributed to the complex terrain around the area of interest that is strongly influencing the vertical wind profile.

Reference wind speed and direction are taken from the reference weather station at $h_{ref} = 28$ m height (10 m above the VATL building, see Fig. 5). The formulations of inlet profiles for air velocity $U(z)$ [m s^{-1}] (Eq. (1)), turbulent kinetic energy $k(z)$ [m^2 s^{-2}] (Eq. (2)), and turbulence dissipation rate $\varepsilon(z)$ [m^2 s^{-3}] (Eq. (3)) are taken from the frequently used conditions provided by Richards and Hoxey [101]. In these relationships, u^*_{ABL} [m s^{-1}] (Eq. (4)) is the Atmospheric Boundary Layer friction velocity [m s^{-1}], κ is the von Karman constant [−] (= 0.42), z is the height coordinate [m], and C_μ is a constant [−] (= 0.09). For determining u^*_{ABL} the wind speed at the boundaries u_b [m s^{-1}] is needed, for which no measurements are available during VP1 and VP2. Therefore, Wieringa's [102] logarithmic transformation equation (Eq. (5)) is used to determine u_b based on the wind speed measured at the reference station u_{ref} [m s^{-1}], the surface roughness at the reference station $z_{0,ref}$ [m], the target height of the transformation h_b [m] and a blending height h_{bh} [m]. In this study, only a transformation due to different roughness lengths is needed, thus h_b is set equal to h_{ref}. The blending height h_{bh} defines the height at which the influence of the ground gets negligible. In Wieringa's work it is taken as 60 m based on a study by Munn and Reimer [103] in Pinawa, Canada. However, in contrast to Trondheim's surrounding, the terrain in both Wieringa's (the Netherlands) and Munn and Reimer's (south-east Manitoba, Canada) studies can be considered as rather flat. There are no measurements of h_{bh} available in Trondheim, but it can be reasonably assumed to be significantly higher than 60 m. It was therefore set to 200 m due to the complex terrain in the area of the computational domain.

$$U(z) = \frac{u^*_{ABL}}{\kappa} \ln\left(\frac{z + z_{0,b}}{z_{0,b}}\right) \tag{1}$$

$$k(z) = \frac{{u^*_{ABL}}^2}{\sqrt{C_\mu}} \tag{2}$$

$$\varepsilon(z) = \frac{{u^*_{ABL}}^3}{\kappa\,(z + z_{0,b})} \tag{3}$$

$$u^*_{ABL} = \frac{\kappa\, u_b}{\ln\left(\frac{h_b + z_{0,b}}{z_{0,b}}\right)} \tag{4}$$

$$u_b = u_{ref}\left[\frac{\ln\left(\frac{h_{bh}}{z_{0,ref}}\right)\ln\left(\frac{h_b}{z_{0,b}}\right)}{\ln\left(\frac{h_{ref}}{z_{0,ref}}\right)\ln\left(\frac{h_{bh}}{z_{0,b}}\right)}\right] \tag{5}$$

The shear condition at the domain top is set to a free-slip condition, assuming zero normal gradients for all the flow variables. To account for longwave radiation losses to the sky, the domain's inlets, outlets and top boundary are assigned a temperature T_{sky} according to Swinbank's [105] simplified correlation (Eq. (6)). As a basis, the air temperature measured at the reference weather station $T_{a,C,ref}$ [°C] is used.

$$T_{sky} = 0.0552\, T^{1.5}_{a,C,ref} \tag{6}$$

2.5. Other computational settings

For the CFD simulations, 3D unsteady Reynolds Averaged Navier Stokes (URANS) equations are applied for which the realisable k-ε turbulence model [106] provides closure. This turbulence model has been used successfully in other validated CFD studies of the urban MC, e.g. Refs. [71,78,80,81,107] and is recommended to use by Franke et al. [93] over the standard k-ε model. Furthermore, it was attributed a generally good performance for wind flow around buildings [24,108,109]. Natural convection is included by using the Boussinesq approximation. The trees are modelled as volumetric porous zones in a spherical shape. This spherical, not perfectly round but to a certain degree irregular shape was created to resemble a "standard" tree crown and was used for all trees in the study area according to their approximate size. For the cells of these porous zones, source/sink terms for the momentum S_{u_i} [Pa m^{-1}] for each velocity component $u_i$with $i = x, y, z$ (Eq. (7), from Refs. [110, 111]), turbulent kinetic energy S_k [kg m^{-1} s^{-3}] (Eq. (8), from Ref. [111]), turbulent dissipation rate S_ε [kg m^{-1} s^{-4}] (Eq. (9), from Ref. [112]) and volumetric heat transfer from evaporation P_c [W m^{-3}] (Eq. (10), from Refs. [80,113,114]) are added:

$$S_{u_i} = -\rho\, LAD\, C_d\, U\, u_i \tag{7}$$

$$S_k = \rho\, LAD\, C_d\, \left(\beta_p\, U^3 - \beta_d\, U\, k\right) \tag{8}$$

$$S_\varepsilon = \rho\, LAD\, C_d \left(C_{\varepsilon 4}\, \beta_p \frac{\varepsilon}{k} U^3 - C_{\varepsilon 5}\, \beta_d\, U\, \varepsilon\right) \tag{9}$$

$$P_{c,trees} = (0.0252\, T_a - 0.078)\, R_h\, LAD \tag{10}$$

In equations (7)–(10), ρ is the density of air [kg m^{-3}], LAD the Leaf Area Density [m^{-1}], C_d the sectional drag for vegetation [−], $(\beta_p, \beta_d, C_{\varepsilon 4}, C_{\varepsilon 5}) = (1.0, 4.0, 0.9, 0.9)$ are model coefficients [−], U the wind speed (across all directions) [m s^{-1}], T_a the air temperature [K], R_h the incoming global solar radiation [W m^{-2}] [115]. The LAD of the trees is selected based on a study by Klingberg et al. [116], who mapped the leaf area of urban greenery using aerial LiDAR (light detection and ranging) and ground-based measurements in Gothenburg, Sweden. The reported LADs for Maples and Chestnuts, very common tree species for the area of interest, were between around 0.6 and 2.1 m^{-1}. Since there are only few

coniferous trees in the explicitly modelled area of the domain, only deciduous trees are used as a simplification. With 1.0 m^{-1}, a slightly lower LAD than the average from Klingberg et al.'s study [116] is applied, as the trees already started to defoliate in the VPs (see Fig. 3).

Many other urban MC CFD studies addressed dense and concrete-dominated city environments [65,71,80,81] and therefore either only included the tree crowns or fully omitted the microclimatic impact of vegetation. Since the NTNU campus is embedded within a park and is surrounded predominantly by single-family homes with gardens (see also Fig. 2), not only the trees but also the evaporative cooling effect from grass-covered soil is expected to significantly impact the microclimatic conditions close to the ground surface. As a consequence, the evapotranspirational cooling effect from short grass canopies was included in the CFD model. For that, the PME is implemented as a user-defined function (UDF) to compute the heat flux from evapotranspiration E [W m^{-2}] which is shown in Eq. (11) [100,117,118].

$$E = \frac{\Delta\ (R_n - G) + \rho\ c_p \frac{D}{r_a}}{\Delta + \gamma \left(1 + \frac{r_s}{r_a}\right)} \tag{11}$$

The PME takes into account the available energy $(R_n - G)$ where R_n is the net radiation [W m^{-2}], G is the soil heat flux [W m^{-2}], D is the vapour pressure deficit of the air [Pa], r_s and r_a are the (bulk) surface and the aerodynamic resistances [s m^{-1}], λ is the latent heat of water vaporization [J kg^{-1}] as calculated from Eq. (12) [119], and γ is the psychrometric constant [Pa K^{-1}], calculated from $P_{atm}\ c_p\ (0.622\ \lambda)^{-1}$, where P_{atm} is the atmospheric pressure [Pa] and c_p is the specific heat capacity of air [J kg^{-1} K^{-1}]. The (bulk) surface resistance r_s and the aerodynamic resistance r_a can be obtained from Eqs. (13) and (14), respectively, where h_{grass} is the height of the grass [m], taken as 0.1 m and r_i is the bulk stomatal resistance of the leaf, taken as $r_i = 100\ s\ m^{-1}$ [120]. The Leaf Area Index (LAI) [−], similar to the volumetric LAD, indicates the available leaf surface area per m^2 vegetated surface, whereas the active Leaf Area Index LAI_{active} [−] takes into consideration that only the upper half of dense clipped grass is actively contributing to the surface heat and vapour transfer. In Eq. (14), $z_{ref,u}$ and $z_{ref,h}$ (both in [m]) are the heights of the wind and humidity measurements, respectively, and u_{ref} is the measured wind speed [m s^{-1}] (in this case at the reference weather station). Although the application of Eq. (14) is restricted to neutral stability conditions where temperature, pressure, and wind velocity follow near adiabatic conditions, it is considered a suitable method for the rough estimation of the cooling flux from evapotranspiration at grass-covered surfaces [120].

$$\lambda = 1.91846\ \times 10^6 \left[\frac{T_{a,C,ref} + 273.15}{T_{a,C,ref} + 239.24}\right]^2 \tag{12}$$

$$r_s = \frac{r_i}{LAI_{active}} = \frac{r_i}{0.5\ LAI} = \frac{r_i}{12\ h_{grass}} \tag{13}$$

$$r_a = \frac{\ln\left[\frac{z_{ref,u} - \frac{2}{3}h_{grass}}{0.123\ h_{grass}}\right] \ln\left[\frac{z_{ref,h} - \frac{2}{3}h_{grass}}{0.0123\ h_{grass}}\right]}{\kappa^2 u_{ref}} \tag{14}$$

The evaporative cooling flux is significantly influenced by the prevailing humidity regime, expressed in Eq. (11) through the slope of the vapour pressure curve Δ [Pa K^{-1}] and the atmospheric vapour pressure deficit D [Pa], calculated from Eqs. (15) and (16), respectively. There, e_{act} is the actual vapour pressure [Pa] and e_{sat} the saturation water pressure [Pa] (see Eq. (17)) for the air temperature $T_{a,C,ref}$ [°C] and relative humidity RH_{ref} [%], as measured from the reference weather station.

$$\Delta = \frac{4098\left[610.8\ exp\left(\frac{17.27\ T_{a,C,ref}}{T_{a,C,ref}+237.3}\right)\right]}{\left(T_{a,C,ref} + 237.3\right)^2} \tag{15}$$

$$D = e_{sat} - e_{act} = \left(1 - RH_{ref}\right)\ e_{sat} \tag{16}$$

$$e_{sat} = \left(1.0007 + 3.46 \times 10^{-8}\ P_{atm}\right)\ 611.21\ exp\left(\frac{\left(18.678 - \frac{T_{a,C,ref}}{234.5}\right) T_{a,C,ref}}{257.14 + T_{a,C,ref}}\right) \tag{17}$$

To facilitate the application of the PME, some simplifications were made. First, the presented CFD model only considers one single phase (only air as a fluid medium) and therefore does not include vapour species transport or evaporation directly. Therefore, the atmospheric vapour pressure deficit D and the slope of the vapour pressure curve δ are calculated as an overall value from the relative humidity RH_{ref} and air temperature $T_{a,C,ref}$ which are recorded at the reference weather station (Eq. (15)–(17)). The same applies to the wind speed u_{ref} in Eq. (14). Therefore, $z_{ref,u}$ and $z_{ref,h}$ are both taken as the height of the reference weather station, which is 28 m above the ground. Second, the available energy for evaporation $(R_n - G)$ is defined as the difference between the net gain from shortwave and longwave radiation R_n and the heat flux into the soil G. For this study, G is neglected in this equation, as for dense canopies such as lawns in a park, its value is relatively small compared to R_n [100]. Third, the atmospheric pressure P_{atm} and the specific heat capacity of air c_p are assumed to be constant and are taken as 101325 Pa and 1008 J kg^{-1} K^{-1}, respectively. The resulting evaporation heat flux is implemented in the CFD model as an internal heat generation rate in the top 1 cm layer of earth at the grass-covered surfaces.

As mentioned before, CFD models can be used to investigate outdoor thermal comfort conditions. For that reason, the standard functionality of ANSYS Fluent is extended with a UDF for calculating the PET [121,122]. According to Fischereit and Schlünzen [123], the PET index is the most frequently used comfort index in obstacle-resolving meteorology models (ORM) such as CFD. They found that it was one among only four out of 165 indices that fulfilled all criteria posed to be applicable in ORMs. To include the PET comfort index in the presented CFD model, the corrected PET equations of the German VDI 3787 [124] from Walther and Goestchel's Python code [125] were translated into C language to make them useable as a UDF in ANSYS Fluent.

The Solar Calculator in ANSYS Fluent was used to determine the sun's position for each time step. Measured values of global horizontal radiation on-site (reference station), divided into direct and diffuse fractions using the approach by Skartveit and Olseth [126] provide the input for the instantaneous solar intensities which are updated once every hour for each time step. Long-wave radiation exchange is incorporated with the discrete ordinates (DO) radiation model [127,128]. For the angular discretization of the DO model, the standard settings for the number of theta and phi divisions are kept at 2, and the number of theta and phi pixels at 1. Pressure-velocity coupling is provided by the SIMPLEC [129] algorithm and schemes of second-order only are used for the spatial discretization.

In this study, two 48-h periods are simulated with 1-h time steps and 400 iterations per time step except for the first one, for which 800 iterations were performed to provide better convergence. As a consequence, in total 48 time steps with 19,600 iterations were carried out for each of the two 48-h periods. On average, the following scaled residuals were reached at the end of each time step in VP1: 6.6×10^{-6} for continuity, 4.0×10^{-5} for x-velocity, 1.6×10^{-5} for y-velocity, 3.6×10^{-5} for z-velocity, 3.8×10^{-4} for k, 9.2×10^{-4} for ε, 2.8×10^{-8} for energy, and 8.0×10^{-7} for radiation. In VP2, the average scaled residuals at the end of each time step were: 3.7×10^{-5} for continuity, 2.2×10^{-4} for x-

velocity, 2.3×10^{-4} for y-velocity, 1.9×10^{-4} for z-velocity, 5.7×10^{-4} for k, 3.6×10^{-3} for ε, 5.0×10^{-8} for energy, and 1.1×10^{-6} for radiation. For comparing simulated with measured values, the simulation results are extracted at the corresponding points of the measurement locations in the domain (see Fig. 5).

3. Results

3.1. Grid-convergence analysis

In this section, the results of the grid-convergence analysis are shown. The grid sizing and computational settings are presented in chapter 2.3. From Fig. 7, it can be seen that the differences between the medium-sized grid, hereafter referred to as the basic grid (9,123,834 cells), and the coarse grid (4,371,409 cells) are relatively small for the measurement points at the weather stations and the additional evaluation lines. Larger grid cells on the walls of the coarser grid, however, resulted in large deviations at the near-wall positions (0.15–0.5 m from the walls).

The differences between the basic and the fine grid (23, 566, 616 cells) on the other hand are so small that a further refinement of the grid would only marginally change the numerical result. The basic grid can be regarded as a good compromise between computational cost and accuracy. Therefore, it was selected for the validation process.

3.2. Simulation results

For evaluating the accordance of the simulation with the measurements, three quality indicators are used: (1) the coefficient of determination (R^2, see Eqs. (18) and (2)) the coefficient of variance of the root mean square deviation (CV_{RMSD}, see Eqs. 19), and (3) the maximum deviation value (D_{max}, see Eq. (20)). In Eqs. (18) and (19), s_i and m_i are the simulated and measured value of time step i, respectively, n is the total number of time steps and $\overline{m}$ is the mean value of measurements.

$$R^2 = 1 - \frac{\sum_{i=0}^{n}(m_i - s_i)^2}{\sum_{i=0}^{n}(m_i - \overline{m})^2} \tag{18}$$

$$CV_{RMSD} = \frac{RMSD}{\overline{m}} \times 100\% = \frac{\sqrt{\sum_{i=1}^{n}(s_i - m_i)/n}}{\overline{m}} \times 100\% \tag{19}$$

$$D_{max} = \max_{i \in \{1,\cdots,n\}} (|s_i - m_i|) \tag{20}$$

In both of the investigated 48-h periods VP1 (September 27–28) and VP2 (October 19–20), the CFD model was able to reproduce the measured conditions at the reference weather station with acceptable accuracy (see Fig. 8 and Fig. 9). Overall, the air temperature is best represented with an R^2 of 0.98 and 0.93, and a CV_{RMSD} of 2.5% and 6.5% for VP1 and VP2 respectively. D_{max} amounted to 0.7 °C in VP1 (28.09. 11:00) and 1.2 °C in VP2 (20.10. 19:00). Both, in VP1 and VP2, the air temperature is slightly underestimated in the simulations.

Simulated wind speed and wind direction also show a satisfactory correlation with the measurements at the reference weather station. In VP1, an R^2 of 0.76 and 0.34 as well as a CV_{RMSD} of 17.3% and 21.9% is obtained for wind speed and direction, respectively. D_{max} is 1.4 m s^{-1} (28.09. 20:00) for the wind speed and 143° (27.09. 11:00) for the wind direction. In VP2, the quality indicators for wind speed and wind direction are 0.44 and 0.91, 38.8% and 14.5%, and 2.1 m s^{-1} (19.10. 14:00) and 99° (20.10. 22:00) for R^2, CV_{RMSD}, and D_{max}, respectively.

The quite large starting threshold of 1 m s^{-1} for both the wind speed and wind direction sensor of the mobile weather stations A–E resulted in a large amount of data falling within the measurement inaccuracy of the sensors. In fact, the measured wind speed at the mobile weather stations was below the sensors' starting threshold 95% and 98% of the time in VP1 and VP2, respectively. For these times, the recorded values are not necessarily zero, but most certainly lower than the actual wind speed at the mobile weather stations A–E. The measured and simulated wind speeds of VP1 and VP2 are shown in Fig. 10. It shows that the measured values are mostly lower than the simulated ones. With exception of only a few data points, the simulated wind speeds lie within the measurement inaccuracy of the sensors.

Comparing measured and simulated wind direction with another was not regarded as meaningful, as low wind speeds will keep the wind direction sensor (a wind vane) for a long time in a steady position that might not be representative of the actual wind direction. During the hourly averaging, these measurements of unrepresentative wind directions then result in unrepresentative values for the respective hours. Other than for the wind speed, the obtained data was not regarded as meaningful for comparison.

Fig. 11 shows the comparison between temperature measurements and simulations at the locations of the mobile weather stations A–E. Similar to the reference weather station, the simulated temperatures show an acceptable agreement with the measurements. The quality indicators of the simulated air temperatures and wind speeds at the locations of the mobile weather stations are summarized in Table 8. Overall, the accordance with the measured values is lower than at the

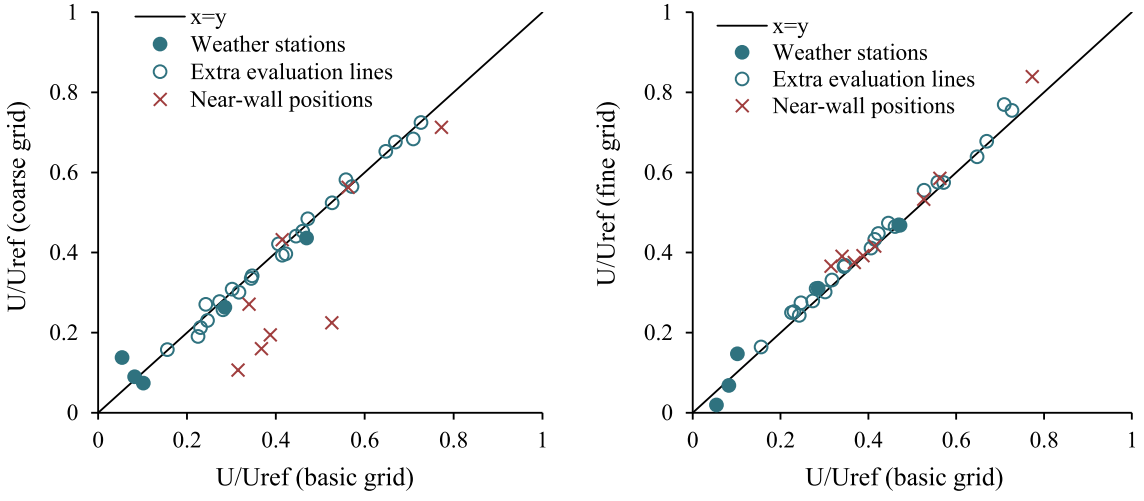

Fig. 7. Comparison of wind speed ratios for the coarse and the basic grid (left) and the fine and the basic grid (right) at the measurement points, the extra evaluation lines, and the near-wall positions.

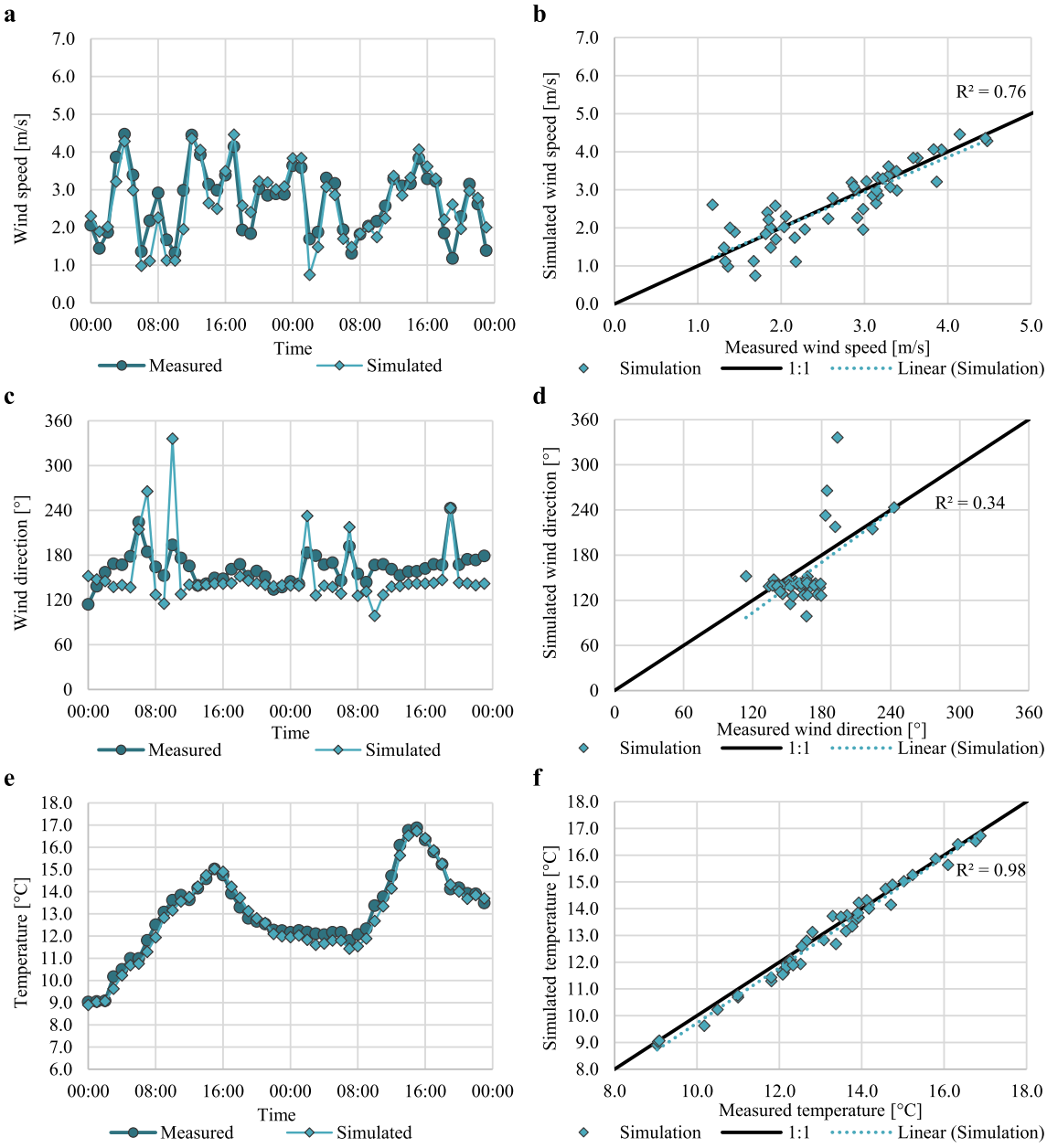

Fig. 8. Comparison of simulated and measured wind speed (a1 and a2), wind direction (c and d) and air temperature (e and f) with error bars indicating the range of measurement uncertainty for September 27–28. Due to the high sensor accuracy, the error bars are hidden behind the data points.

reference weather station. Regarding air temperature, a more pronounced underestimation of the simulated values is noticeable at the mobile weather stations compared to the reference weather station. This is especially the case during the second day of VP1 (high amount of solar irradiation) at station B which is located between trees and on a large lawn. At weather station D, the accordance with measured air temperature is best, both for VP1 and VP2. Note that station D is the only weather station which is not placed on grass but on concrete pavement. Although the quality indicators of the simulated wind speed in Fig. 10 give the impression of a poor fit, it needs to be taken into consideration that the simulated values are almost always within the sensors' uncertainty of measurement.

4. Discussion

4.1. Interpretation of results

When looking at the simulation results and the quality indicators at the reference weather station, especially the differences of wind speed and direction between VP1 and VP2 stand out. In VP1, the wind speed ($R^2 = 0.76$, $CV_{RMSD} = 17.3\%$, $D_{max} = 1.4$ m s^{-1}) is much better represented than wind direction ($R^2 = 0.34$, $CV_{RMSD} = 21.9\%$, $D_{max} = 143°$). In VP2 on the other hand, the correlation between simulated and measured wind speed ($R^2 = 0.44$, $CV_{RMSD} = 38.8\%$, $D_{max} = 2.1$ m s^{-1}) is significantly lower than the correlation between simulated and measured wind direction ($R^2 = 0.91$, $CV_{RMSD} = 14.5\%$, $D_{max} = 98°$).

These differences can be partly explained by the influence of the hilly terrain which is higher towards the east and lower towards the west of the campus. With a prevailing southern wind direction, the air flow is deflected to a more south-eastern wind direction by the higher terrain to

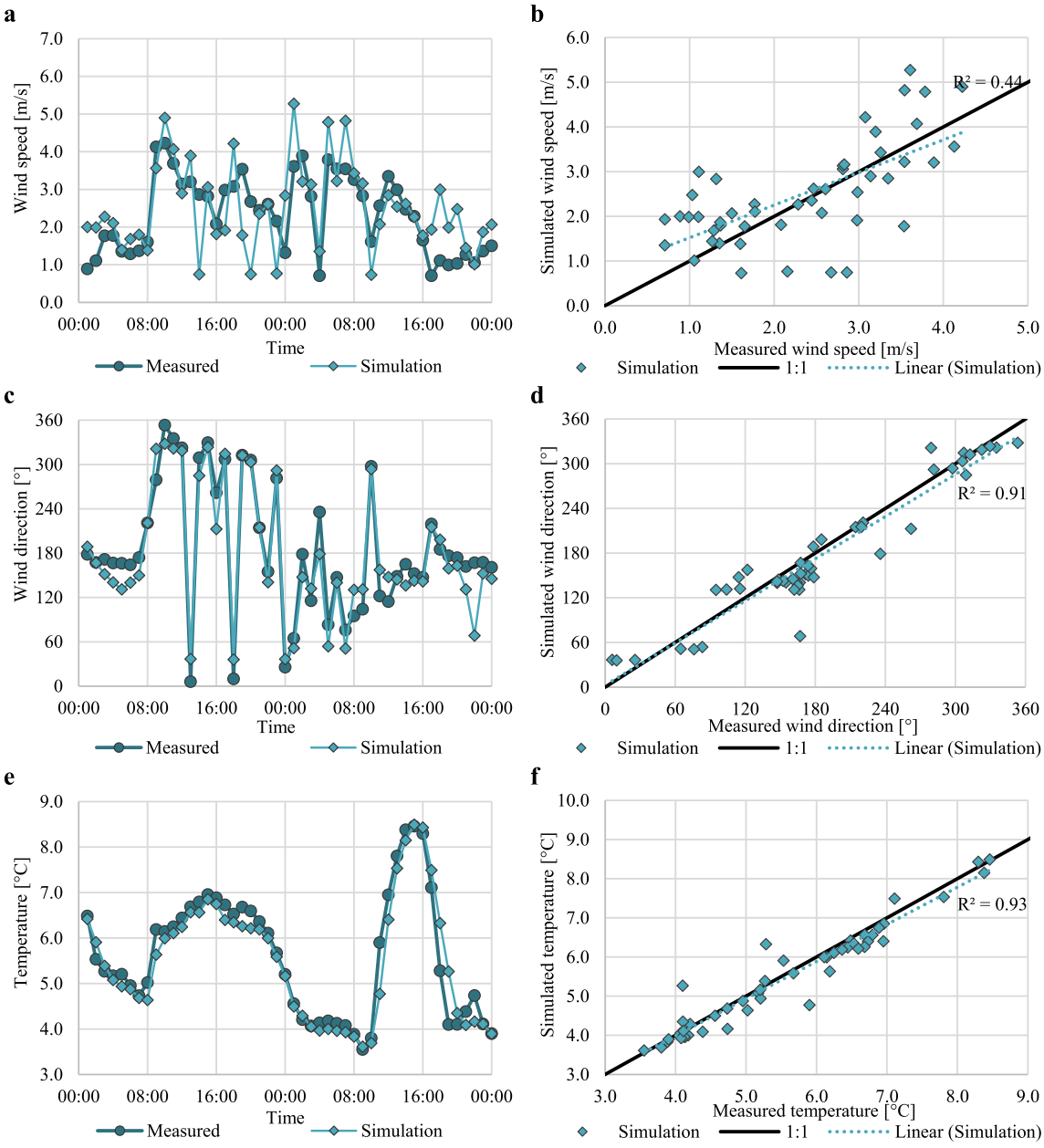

Fig. 9. Comparison of simulated and measured wind speed (a and b), wind direction (c and d) and air temperature (e and f) with error bars indicating the range of measurement uncertainty for October 19–20. Due to the high sensor accuracy, the error bars are hidden behind the data points.

the east (represented in grey in Fig. 12). This effect can be seen throughout VP1 where simulated wind directions are constantly below the recorded (input) values at measured wind directions from 150° to 180° (see the accumulation of datapoints below the 1:1 line between 150° and 180° in Fig. 8d). The same applies to the respective times in VP2, as indicated for instance at the first seven and last six time steps of the simulation (see Fig. 9c and the accumulation of datapoints below the 1:1 line between 150° and 180° in Fig. 9d). Moreover, it cannot be ruled out that the inlet reference measurement data from these angles were influenced by this phenomenon and that the true wind directions at the domain inlet, located about 2 km south of the campus, were at slightly higher angles than the ones used.

However, the CFD model proved to be able to represent the wind direction adequately over the whole spectrum of the wind directions, especially during VP2. There, the wind was blowing less often from these wind directions between 150° and 180° and more from directions that are generally better represented. Therefore, the quality indicators and overall accordance between simulated and measured values are much better.

Analogously, using the recorded wind speed from the reference weather station as a basis for the inlet profiles in the CFD simulations certainly introduces an error to the simulations. Even though the reference weather station is located 10 m above the roof of a large building, it is still about 20 m below the roof height of the two central buildings to the south (building SB1 and SB2) and 4 m below the roof height of the much closer main building to the north-west (building HB). These buildings create significant turbulences and have large wakes that most likely impact the measurements at the reference weather station (see Fig. 12).

There are several points in time when the reference weather station is in the wake of building HB during westerly and north-westerly winds (VP2 19.10 at 14:00, 17:00, 19:00, 20:00, 23:00 and 20.10 at 10:00). It is likely that the measurements are taken within the wake of this building and are thus lower than the actual free-stream air velocities.

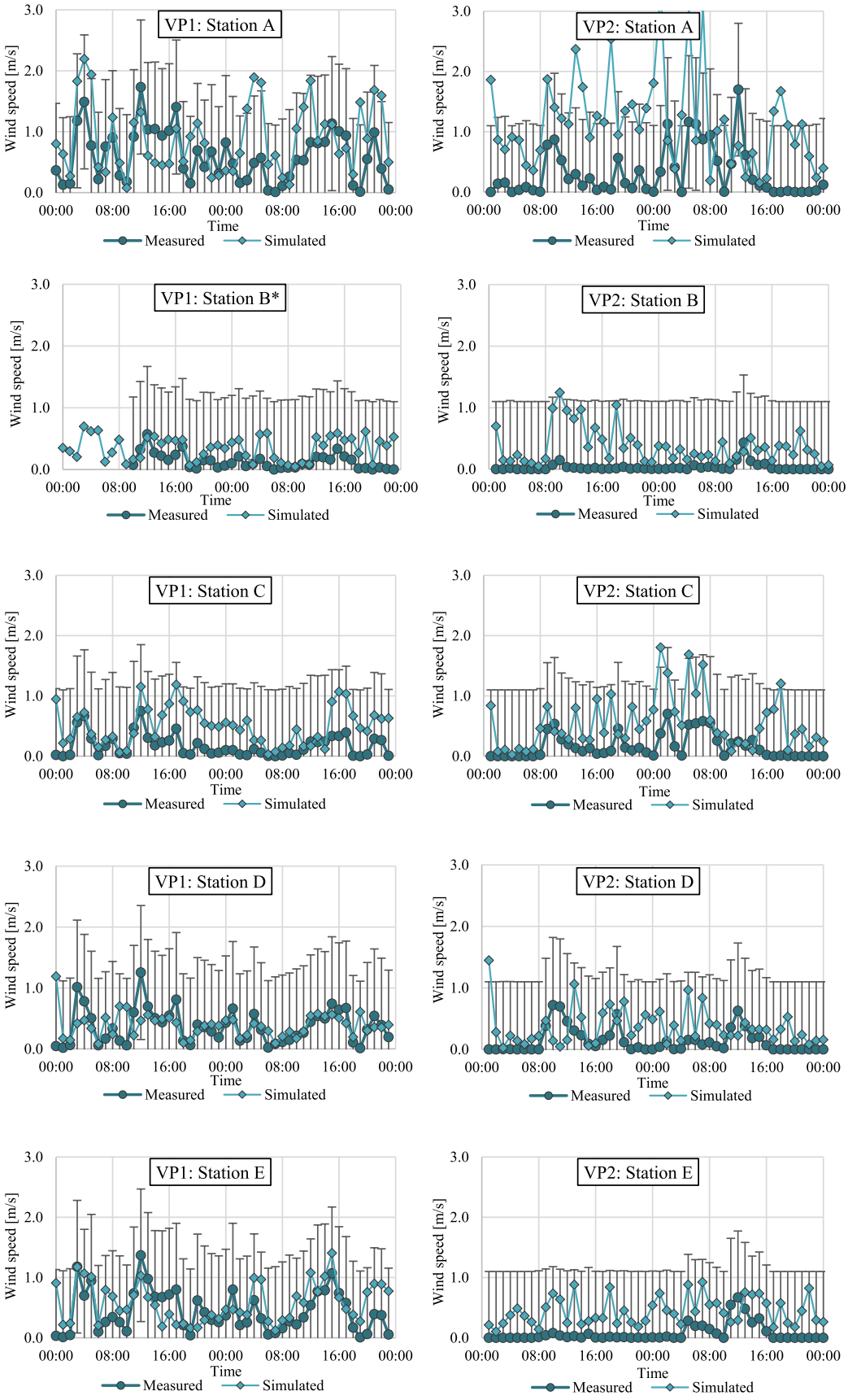

Fig. 10. Comparison of simulated and measured wind speed with error bars indicating the range of measurement uncertainty at the mobile weather stations for VP1 (left) and VP2 (right). *Because of a sensor failure during VP1, the records of the first 9 h of Station B are missing.

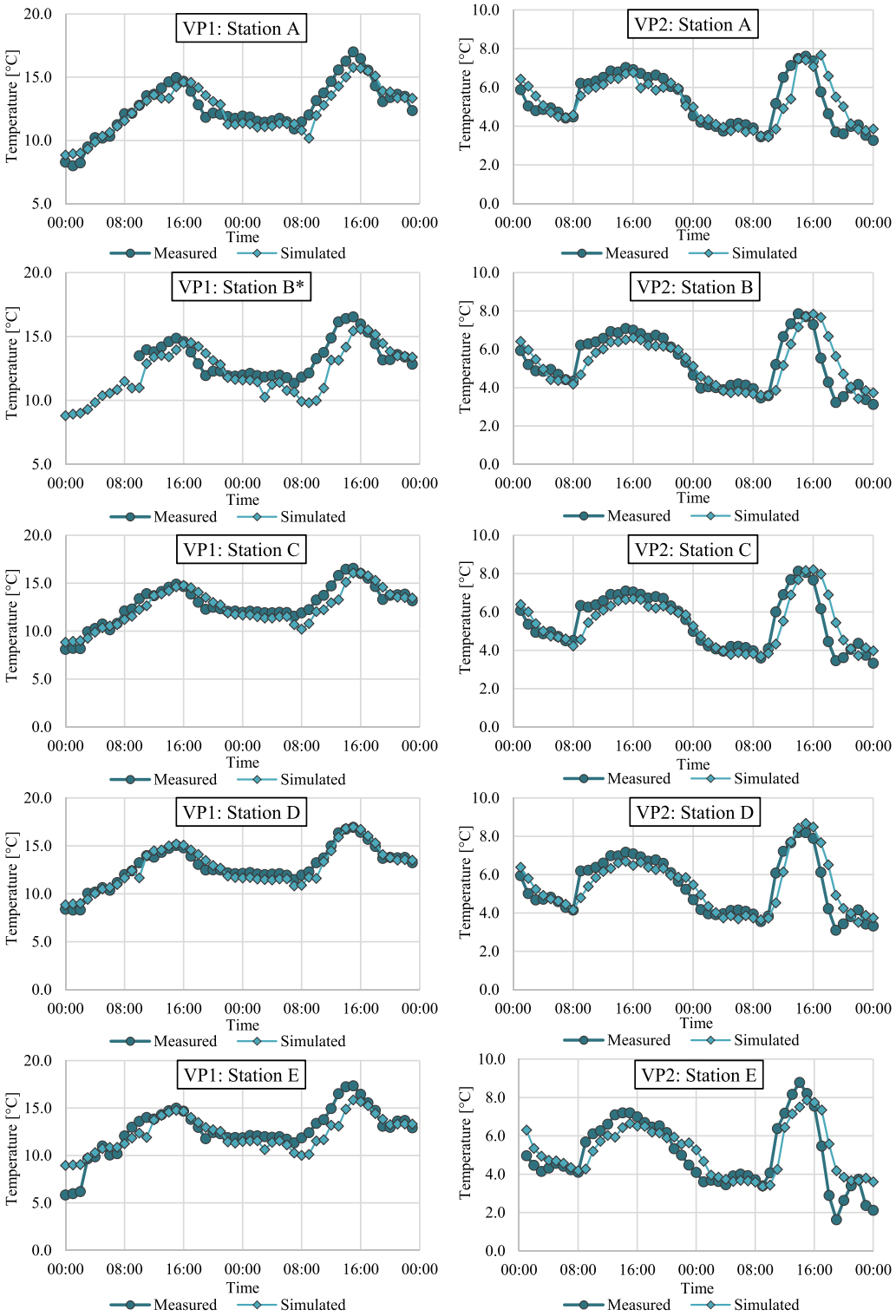

Fig. 11. Comparison of simulated and measured air temperature with error bars indicating the range of measurement uncertainty at the mobile weather stations for VP1 (left) and VP2 (right). Due to the high sensor accuracy, the error bars are hidden behind the data points. *Because of a sensor failure during VP1, the records of the first 9 h of Station B are missing.

Using such measurements as a basis for determining the inlet profiles in the CFD simulations, where data is again extracted within the wake of the building, can lead to significantly lower wind speeds than measured. However, despite wind coming from a similar wind direction, at other time steps the agreement is quite fair (VP2 19.10. at 11:00, 12:00, 15:00). A possible reason for that might be the choice of turbulence model that has a significant impact on the flow variables in wakes behind obstacles, as they determine the wakes' size and extent [109]. Even a slightly different shape of the wake can lead to significant discrepancies between simulation results and measurements as the gradients of the flow variables are usually very high at such locations [130]. In the context of this study, however, no comparison of different turbulence models was made.

As in the simulations, data can be extracted without significant

Table 8
Quality indicators R^2, CV_{RMSD} and D_{max} of the simulated air temperatures and wind speeds at the locations of the mobile weather stations. The best-obtained correlation to measured values in the respective validation periods (VP) and the respective quality indicators are marked in bold.

	Validation Period	Quality indicator	Station A	Station B	Station C	Station D	Station E
Wind Speed	VP1	R^2	0.16	0.20	0.26	0.06	**0.29**
		CV_{RMSD}	102.4%	210.4%	244.3%	82.3%	**80.0%**
		D_{max}	1.5 m s^{-1}	**0.6 m s^{-1}**	0.9 m s^{-1}	1.1 m s^{-1}	0.9 m s^{-1}
	VP2	R^2	0.01	0.02	**0.25**	0.00	0.07
		CV_{RMSD}	383.3%	1388.7%	335.6%	**300.7%**	571.8%
		D_{max}	3.0 m s^{-1}	1.1 m s^{-1}	1.4 m s^{-1}	1.4 m s^{-1}	**0.9 m s^{-1}**
Temperature	VP1	R^2	0.86	0.49	0.83	**0.93**	0.75
		CV_{RMSD}	6.3%	10.2%	6.8%	**4.5%**	10.5%
		D_{max}	1.8 °C	3.3 °C	2.5 °C	**1.6 °C**	3.4 °C
	VP2	R^2	0.68	0.64	0.69	**0.76**	0.69
		CV_{RMSD}	14.0%	15.7%	14.1%	**13.5%**	19.5%
		D_{max}	1.9 °C	2.4 °C	2.4 °C	2.3 °C	2.7 °C

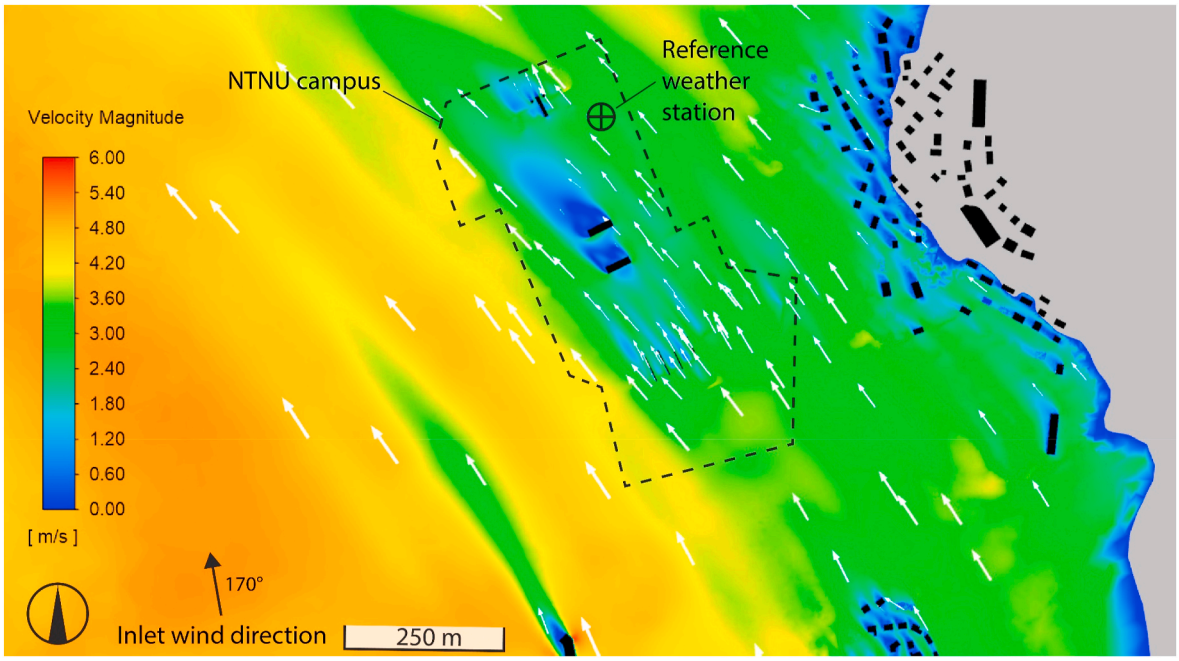

Fig. 12. View from the top at a horizontal cut through the domain at 73.66 m (height of the reference weather station above sea level) showing the velocity magnitude on September 28, at 05:00. The terrain above the cutting plane is visualized in grey.

limitations regarding sensitivity at the control points, simulated wind speeds at the locations of the mobile weather stations A–E are mostly higher than the measurements (see Fig. 10). It must be noted that the simulated values are almost always within the sensors' measurement uncertainty and follow largely the same course as the measurements, particularly at stations B–E in VP1. Hence, considering the large uncertainty of measurements especially below 1 m s^{-1}, the CFD model can be regarded as suitable to predict the wind speeds at the low-level atmospheric boundary layer with acceptable accuracy.

The best-represented climate variable in the simulations is the air temperature with overall good accordance of simulated and measured values at all locations. However, the underestimation of air temperatures is more pronounced closer to the ground at the mobile weather stations compared to the reference weather station. This is especially visible during times of high solar irradiation like on the second day of VP1 (28.09.) It is also noticeable that weather station D, the only mobile station that is not standing on a patch of grass, shows the best accordance with measurements during VP1 and VP2 among the mobile stations. This supports the assumption that the way the Penman-Monteith equation was applied in this research is overestimating the cooling flux from evapotranspiration from the grass surfaces and that adjustment is necessary.

Aside from the CFD model-specific causes for deviations between simulation results and measurements, several factors are generally introducing errors to the simulations. These are for instance geometrical inaccuracies [131] and discretization errors [93,132], the choice of materials and their properties, and the omission of water vapour transfer. Furthermore, inaccuracies related to the choice of inlet profiles for U, k, and ε, or the major detriments that come along with using URANS and a 2-equation turbulence model in the first place are generally considerable sources of errors.

As mentioned before, the underlying geometry of the CFD model is based on a large urban 3D geometrical city model from Trondheim municipality and LiDAR data, containing the terrain and buildings of the area. However, the data did not contain relatively small elements like bus stops, street poles and signs, small garden sheds etc. Furthermore, the surrounding buildings' geometries were simplified by the authors into boxes, omitting complex roof structures, balconies, oriels, and protrusions etc. to limit the computational cost. Their influence on the flow regime was estimated to be negligible based on the work by Ricci et al. [131]. Only when located directly on campus, trees and larger vegetation was included in the geometry.

In this research, the urban surface was grouped into categories of dominant materials (see Fig. 5), in order to limit the time needed for

creating the CFD model and still keep it relatively easy to use. The real urban surface on the other hand is extremely complex and usually composed of a large variety of different materials, colours, and a mix of different plants, each having an individual and heterogenic shape, aerodynamic properties and stomatal characteristics. Additionally, water vapour transfer was only indirectly considered in this work. While water runoff or retention properties of the urban surface and multiphase models were not incorporated in this simulation model, solely the thermal effect of evapotranspiration from the trees and grass were included according to Eq. (10) and Eq. (11).

Richards' and Hoxey's [101] profile for U, k and ε were used in this work, following the practice of many other CFD studies in the urban environment [65,71,78,80,81,133]. These inlet profiles were originally derived for the neutrally stratified atmospheric boundary layer for a uniform fetch of at least 5 km and their applicability in complex terrains like the study area in this research can be questioned. However, as no

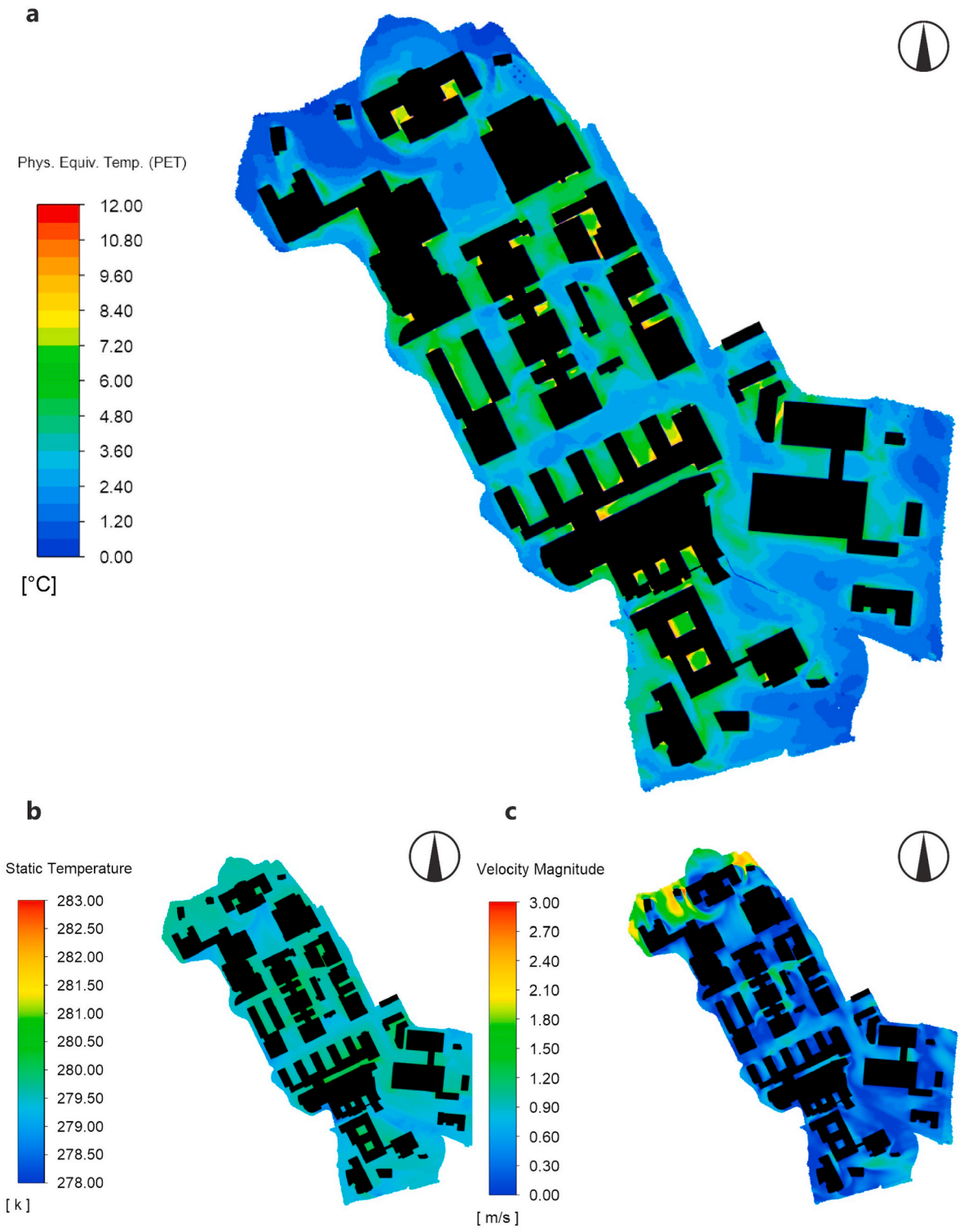

Fig. 13. Simulation results for: a) Physiological Equivalent Temperature (PET), b) air temperature and c) wind speed at 1.75 m height above ground in the study area at 19.10. at 15:00.

measurements near the four lateral domain boundaries were available, the commonly used profiles from Richards and Hoxey [101] represented the best assumption for the inlet profiles in this study. Yet in summary, the presented validation results and overall good fit of measured and simulated values clearly indicate that the benefits from using this CFD model overweigh the uncertainties connected to the input.

4.2. Applicability of the CFD model

Despite the limitations and uncertainties related to the input that can hardly be eliminated completely, the presented CFD model is well suited to be used for predicting the urban microclimatic conditions in the study area. One of the possible applications can be the evaluation of outdoor thermal comfort. Fig. 13 shows the PET, air temperature and wind speed at 1.75 m height on October 19 at 15:00 in the study area. It is noticeable that areas with a low PET coincide with areas of high wind speed, especially in the north/north-west of the campus. In the central part of the study area, however, the PET is higher on average. The highest values are computed close to the buildings and in their inside corners. There, particularly low air velocity combined with heat transfer from the buildings result in better outdoor thermal comfort conditions. Moreover, a clear correlation between the surface material and the PET can be seen. Particularly the grass patches on which the mobile weather stations B and E are located, exhibit a quite low PET.

Fig. 14 shows the solar irradiation on 19.10. at 15:00 in the central, explicitly modelled area of the domain, as viewed from the south. The shadow cast from the hill on which the campus is located is clearly visible on the north-eastern side of the campus. The slope of the hill facing south-west, on the other hand, receives almost twice as much solar radiation. Furthermore, the shadows from the geometrically explicitly modelled trees are clearly visible as blue dots on this slope. The highest solar heat flux is received on building façades facing south-west at the illustrated point in time.

5. Conclusion

In this study, the validation process of a CFD model, applying the 3D URANS approach with the realisable k-ε turbulence model of a highly complex urban area around the NTNU campus in Trondheim, Norway, was presented. The CFD model features a polyhedral grid of the urban environment, including geometrically explicitly modelled buildings and trees within the area of interest, solar and longwave radiation exchange, heat transfer from the buildings, heat storage, and the thermal effects of evapotranspiration from the trees and grass.

To validate the CFD model, a network of six weather stations, of which five were mobile, provided hourly-averaged measurements for wind speed, wind direction and air temperature. Two 48-h validation periods (VP1 and VP2) during the measurement campaign were selected that contained one sunny day, with relatively strong fluctuations and a high average of wind speed, a pronounced diurnal temperature variation and a large variation of wind direction. These criteria were established to test the CFD model's performance under demanding and a large variety of conditions.

Hourly-averaged measurements from the reference weather station were used as a reference for the empirical inlet profiles fed into the CFD model and always two of the lateral boundaries were set as inlets and outlets according to the wind direction. Overall, the CFD model was capable of reproducing the measured conditions at the location of the reference weather station with acceptable accuracy.

As the measured wind direction data was strongly affected by measurement uncertainty due to the sensor threshold of the five mobile weather stations, only temperature and wind speed data from the mobile stations was used in the validation assessment. Yet, all three climate variables served as validation variables at the reference weather station. Overall, the air temperature at the reference weather station was best represented with an R^2 of 0.98 and 0.93, and a CV_{RMSD} of 2.5% and 6.5% for VP1 and VP2 respectively. D_{max} amounted to 0.4 °C in VP1 and 1.2 °C in VP2. Also, at the mobile weather stations, air temperature was well represented during both VPs with an R^2, CV_{RMSD}, and D_{max} of 0.49–0.93, 4.5–19.5% and 1.6–3.4 °C, respectively.

Simulated wind speed and wind direction also showed a satisfactory correlation with the measurements at the reference weather station. In VP1, an R^2 of 0.76 and 0.34 as well as a CV_{RMSD} of 17.3% and 21.9% were obtained for wind speed and direction, respectively. D_{max} was 1.4 m s^{-1} for the wind speed and 143° for the wind direction. In VP2, the quality indicators for wind speed and wind direction were 0.44 and 0.91, 38.8% and 14.5%, and 2.1 m s^{-1} and 98° for R^2, CV_{RMSD}, and D_{max}, respectively. At the mobile weather stations, only the simulated wind speeds were compared to the measurements. Even though the quality metrics did not indicate an acceptable fit, the simulation results were almost entirely within the wind sensors' measurement uncertainty. From that, it can be concluded that the low-level atmospheric boundary layer wind speeds are represented by the CFD model with sufficient accuracy. Hence, the presented CFD model can be used for its intended purpose of evaluating the urban MC in the study area in future studies.

It was observed that the PME slightly overestimated the cooling flux from evapotranspiration at grass-covered surfaces, as the comparison between simulated and measured air temperatures indicated and underestimation of the temperature at the mobile weather stations (3.0 m above ground) compared to the reference weather station (28 m above

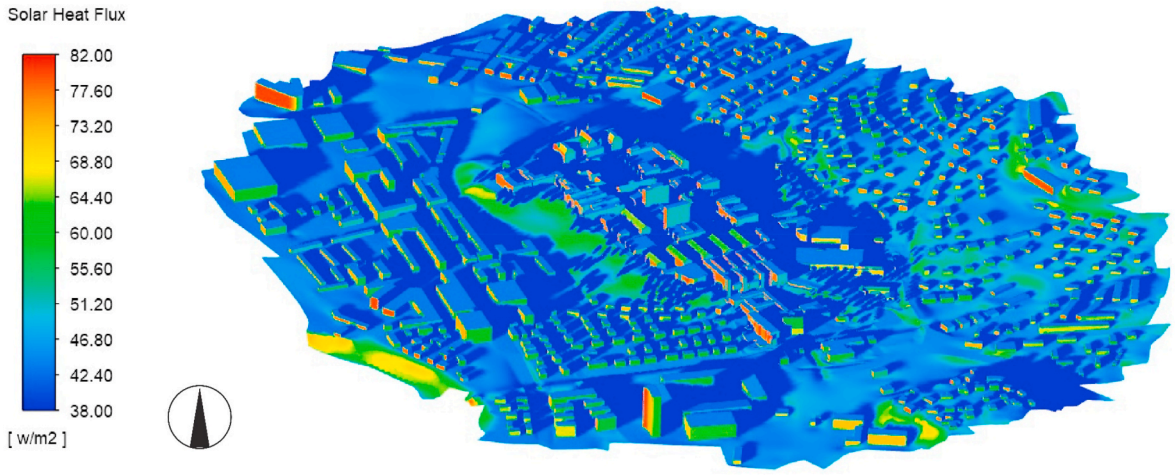

Fig. 14. Solar heat flux in the central, explicitly modelled part of the domain for 19.10. at 15:00 with view from south.

ground). Furthermore, the mobile weather stations standing on patches of grass gave the largest underestimation.

It can be concluded that the presented CFD model has the potential to predict urban microclimatic conditions in the study area with acceptable accuracy. It can be utilized in future studies focusing for instance on the influence of the urban fabric and vegetation on the energy use in buildings, outdoor thermal comfort, pedestrian wind comfort, pollutant dispersion, pressure coefficients on building façades for the natural ventilation potential, or urban wind energy potential. At the same time, more studies focusing on the wind regime in and around Trondheim need to be carried out in order to derive location-specific profiles for CFD inlet conditions. Future studies should also evaluate the impact of different turbulence models on the CFD model's ability to predict the airflow at the NTNU campus.

Declaration of competing interest

The authors declare that they have no known competing financial interests or personal relationships that could have appeared to influence the work reported in this paper.

Acknowledgements

This paper has been written within the Research Centre on Zero Emission Neighbourhoods in Smart Cities (FME ZEN). The authors gratefully acknowledge the support from the ZEN partners and the Research Council of Norway. The simulations were performed on resources provided by UNINETT Sigma2 - the National Infrastructure for High Performance Computing and Data Storage in Norway.

References

[1] O. Edenhofer (Ed.), Climate Change 2014: Mitigation of Climate Change Working Group III Contribution to the Fifth Assessment Report of the Intergovernmental Panel on Climate Change, Cambridge University Press, New York (USA), 2014.
[2] United Nations, Department of Economic, Social Affairs, Population Division, World Urbanization Prospects: the 2018 Revision, Online Edition, New York, USA, 2018.
[3] G. Mills, Urban climatology: history, status and prospects, Urban Clim. 10 (2014) 479–489, https://doi.org/10.1016/j.uclim.2014.06.004.
[4] Y. Toparlar, B. Blocken, B. Maiheu, G. van Heijst, A review on the CFD analysis of urban microclimate, Renew. Sustain. Energy Rev. 80 (2017) 1613–1640, https://doi.org/10.1016/j.rser.2017.05.248.
[5] P.A. Mirzaei, F. Haghighat, Approaches to study urban heat island – abilities and limitations, Build. Environ. 45 (10) (2010) 2192–2201, https://doi.org/10.1016/j.buildenv.2010.04.001.
[6] I. Orlanski, A rational subdivision of scales for atmospheric processes, Bull. Am. Meteorol. Soc. 56 (5) (1975) 527–530.
[7] T.R. Oke, Urban heat islands, in: I. Douglas, D. Goode, M. Houck, D. Maddox (Eds.), The Routledge Handbook of Urban Ecology, first ed., Routledge, London, 2011, pp. 120–131.
[8] T.R. Oke, The energetic basis of the urban heat island, Q. J. Roy. Meteorol. Soc. 108 (455) (1982) 1–24, https://doi.org/10.1002/qj.49710845502.
[9] G.J. Steeneveld, S. Koopmans, B.G. Heusinkveld, L.W.A. van Hove, A.A. M. Holtslag, Quantifying urban heat island effects and human comfort for cities of variable size and urban morphology in The Netherlands, J. Geophys. Res. 116 (D20) (2011) 94, https://doi.org/10.1029/2011JD015988.
[10] R. Watkins, J. Palmer, M. Kolokotroni, Increased temperature and intensification of the urban heat island: implications for human comfort and urban design, Built. Environ. 33 (1) (2007) 85–96, https://doi.org/10.2148/benv.33.1.85.
[11] A. Urban, H. Davídkovová, J. Kyselý, Heat- and cold-stress effects on cardiovascular mortality and morbidity among urban and rural populations in the Czech Republic, Int. J. Biometeorol. 58 (6) (2014) 1057–1068, https://doi.org/10.1007/s00484-013-0693-4.
[12] D. D'Ippoliti, P. Michelozzi, C. Marino, F. de'Donato, B. Menne, K. Katsouyanni, et al., The impact of heat waves on mortality in 9 European cities: results from the EuroHEAT project, Environ. Health 9 (2010) 37, https://doi.org/10.1186/1476-069X-9-37.
[13] M. Davies, P. Steadman, T. Oreszczyn, Strategies for the modification of the urban climate and the consequent impact on building energy use, Energy Pol. 36 (12) (2008) 4548–4551, https://doi.org/10.1016/j.enpol.2008.09.013.
[14] M. Kolokotroni, I. Giannitsaris, R. Watkins, The effect of the London urban heat island on building summer cooling demand and night ventilation strategies, Sol. Energy 80 (4) (2006) 383–392, https://doi.org/10.1016/j.solener.2005.03.010.
[15] E. Vardoulakis, D. Karamanis, A. Fotiadi, G. Mihalakakou, The urban heat island effect in a small Mediterranean city of high summer temperatures and cooling energy demands, Sol. Energy 94 (2013) 128–144, https://doi.org/10.1016/j.solener.2013.04.016.
[16] S.A. Lowe, An energy and mortality impact assessment of the urban heat island in the US, Environ. Impact Assess. Rev. 56 (2016) 139–144, https://doi.org/10.1016/j.eiar.2015.10.004.
[17] V.V. Klimenko, A.S. Ginzburg, P.F. Demchenko, A.G. Tereshin, I.N. Belova, E. V. Kasilova, Impact of urbanization and climate warming on energy consumption in large cities, Dokl. Phys. 61 (10) (2016) 521–525, https://doi.org/10.1134/S1028335816100050.
[18] T.R. Oke, G. Mills, A. Christen, J.A. Voogt, Urban Climates, Cambridge University Press, Cambridge, 2017.
[19] D. Chapman, K. Nilsson, A. Larsson, A. Rizzo, Climatic barriers to soft-mobility in winter: luleå, Sweden as case study, Sustain. Cities Soc. 35 (2017) 574–580, https://doi.org/10.1016/j.scs.2017.09.003.
[20] E. Erell, D. Pearlmutter, T. Williamson, Urban Microclimate: Designing the Spaces between Buildings, Earthscan, London, 2011.
[21] B. Blocken, Computational Fluid Dynamics for urban physics: importance, scales, possibilities, limitations and ten tips and tricks towards accurate and reliable simulations, Build. Environ. 91 (2015) 219–245, https://doi.org/10.1016/j.buildenv.2015.02.015.
[22] B. Blocken, W.D. Janssen, T. van Hooff, CFD simulation for pedestrian wind comfort and wind safety in urban areas: general decision framework and case study for the Eindhoven University campus, Environ. Model. Software 30 (2012) 15–34, https://doi.org/10.1016/j.envsoft.2011.11.009.
[23] B. Blocken, J. Persoon, Pedestrian wind comfort around a large football stadium in an urban environment: CFD simulation, validation and application of the new Dutch wind nuisance standard, J. Wind Eng. Ind. Aerod. 97 (5–6) (2009) 255–270, https://doi.org/10.1016/j.jweia.2009.06.007.
[24] B. Blocken, S. Roels, J. Carmeliet, Modification of pedestrian wind comfort in the Silvertop Tower passages by an automatic control system, J. Wind Eng. Ind. Aerod. 92 (10) (2004) 849–873, https://doi.org/10.1016/j.jweia.2004.04.004.
[25] W.D. Janssen, B. Blocken, T. van Hooff, Pedestrian wind comfort around buildings: comparison of wind comfort criteria based on whole-flow field data for a complex case study, Build. Environ. 59 (2013) 547–562, https://doi.org/10.1016/j.buildenv.2012.10.012.
[26] M.S. Fadl, J. Karadelis, CFD simulation for wind comfort and safety in urban area: a case study of coventry university central campus, Int. J. Archit. Eng. Constr. 2 (2) (2013) 131–143, https://doi.org/10.7492/IJAEC.2013.013.
[27] C. Gromke, B. Blocken, Influence of avenue-trees on air quality at the urban neighborhood scale. Part I: quality assurance studies and turbulent Schmidt number analysis for RANS CFD simulations, Environ. Pollut. 196 (2015) 214–223, https://doi.org/10.1016/j.envpol.2014.10.016.
[28] C. Gromke, B. Blocken, Influence of avenue-trees on air quality at the urban neighborhood scale. Part II: traffic pollutant concentrations at pedestrian level, Environ. Pollut. 196 (2015) 176–184, https://doi.org/10.1016/j.envpol.2014.10.015.
[29] J.H. Amorim, V. Rodrigues, R. Tavares, J. Valente, C. Borrego, CFD modelling of the aerodynamic effect of trees on urban air pollution dispersion, Sci. Total Environ. 461–462 (2013) 541–551, https://doi.org/10.1016/j.scitotenv.2013.05.031.
[30] P. Gousseau, B. Blocken, T. Stathopoulos, G. van Heijst, CFD simulation of near-field pollutant dispersion on a high-resolution grid: a case study by LES and RANS for a building group in downtown Montreal, Atmos. Environ. 45 (2) (2011) 428–438, https://doi.org/10.1016/j.atmosenv.2010.09.065.
[31] B. Blocken, J. Carmeliet, The influence of the wind-blocking effect by a building on its wind-driven rain exposure, J. Wind Eng. Ind. Aerod. 94 (2) (2006) 101–127, https://doi.org/10.1016/j.jweia.2005.11.001.
[32] B. Blocken, J. Carmeliet, Validation of CFD simulations of wind-driven rain on a low-rise building facade, Build. Environ. 42 (7) (2007) 2530–2548, https://doi.org/10.1016/j.buildenv.2006.07.032.
[33] T. van Hooff, B. Blocken, M. van Harten, 3D CFD simulations of wind flow and wind-driven rain shelter in sports stadia: influence of stadium geometry, Build. Environ. 46 (1) (2011) 22–37, https://doi.org/10.1016/j.buildenv.2010.06.013.
[34] H. Chen, R. Ooka, H. Huang, T. Tsuchiya, Study on mitigation measures for outdoor thermal environment on present urban blocks in Tokyo using coupled simulation, Build. Environ. 44 (11) (2009) 2290–2299, https://doi.org/10.1016/j.buildenv.2009.03.012.
[35] C.-M. Hsieh, H. Chen, R. Ooka, J. Yoon, S. Kato, K. Miisho, Simulation analysis of site design and layout planning to mitigate thermal environment of riverside residential development, Build. Simul. 3 (1) (2010) 51–61, https://doi.org/10.1007/s12273-010-0306-7.
[36] W.T. Chow, A.J. Brazel, Assessing xeriscaping as a sustainable heat island mitigation approach for a desert city, Build. Environ. 47 (2012) 170–181, https://doi.org/10.1016/j.buildenv.2011.07.027.
[37] M.F. Shahidan, P.J. Jones, J. Gwilliam, E. Salleh, An evaluation of outdoor and building environment cooling achieved through combination modification of trees with ground materials, Build. Environ. 58 (2012) 245–257, https://doi.org/10.1016/j.buildenv.2012.07.012.
[38] E. Carnielo, M. Zinzi, Optical and thermal characterisation of cool asphalts to mitigate urban temperatures and building cooling demand, Build. Environ. 60 (2013) 56–65, https://doi.org/10.1016/j.buildenv.2012.11.004.
[39] M. Srivanit, K. Hokao, Evaluating the cooling effects of greening for improving the outdoor thermal environment at an institutional campus in the summer, Build. Environ. 66 (2013) 158–172, https://doi.org/10.1016/j.buildenv.2013.04.012.

[40] W. Su, Y. Zhang, Y. Yang, G. Ye, Examining the impact of greenspace patterns on land surface temperature by coupling LiDAR data with a CFD model, Sustainability 6 (10) (2014) 6799–6814, https://doi.org/10.3390/su6106799.
[41] M. Taleghani, D.J. Sailor, M. Tenpierik, A. van den Dobbelsteen, Thermal assessment of heat mitigation strategies: the case of Portland State University, Oregon, USA, Build. Environ. 73 (2014) 138–150, https://doi.org/10.1016/j.buildenv.2013.12.006.
[42] Y. Tominaga, Y. Sato, S. Sadohara, CFD simulations of the effect of evaporative cooling from water bodies in a micro-scale urban environment: validation and application studies, Sustain. Cities Soc. 19 (2015) 259–270, https://doi.org/10.1016/j.scs.2015.03.011.
[43] Y. Wang, H. Akbari, Analysis of urban heat island phenomenon and mitigation solutions evaluation for Montreal, Sustain. Cities Soc. 26 (2016) 438–446, https://doi.org/10.1016/j.scs.2016.04.015.
[44] U. Berardi, The outdoor microclimate benefits and energy saving resulting from green roofs retrofits, Energy Build. 121 (2016) 217–229, https://doi.org/10.1016/j.enbuild.2016.03.021.
[45] Y. Kim, S. An, J.-H. Eum, J.-H. Woo, Analysis of thermal environment over a small-scale landscape in a densely built-up asian megacity, Sustainability 8 (4) (2016) 358, https://doi.org/10.3390/su8040358.
[46] Y. Wang, U. Berardi, H. Akbari, Comparing the effects of urban heat island mitigation strategies for Toronto, Canada, Energy Build. 114 (2016) 2–19, https://doi.org/10.1016/j.enbuild.2015.06.046.
[47] G.-E. Kyriakodis, M. Santamouris, Using reflective pavements to mitigate urban heat island in warm climates - results from a large scale urban mitigation project, Urban Clim. 24 (1) (2018) 326–339, https://doi.org/10.1016/j.uclim.2017.02.002.
[48] N. Fintikakis, N. Gaitani, M. Santamouris, M. Assimakopoulos, D. N. Assimakopoulos, M. Fintikaki, et al., Bioclimatic design of open public spaces in the historic centre of Tirana, Albania, Sustain. Cities Soc. 1 (1) (2011) 54–62, https://doi.org/10.1016/j.scs.2010.12.001.
[49] N. Gaitani, A. Spanou, M. Saliari, A. Synnefa, K. Vassilakopoulou, K. Papadopoulou, et al., Improving the microclimate in urban areas: a case study in the centre of Athens, Build. Serv. Eng. Technol. 32 (1) (2011) 53–71, https://doi.org/10.1177/0143624410394518.
[50] M. Santamouris, N. Gaitani, A. Spanou, M. Saliari, K. Giannopoulou, K. Vasilakopoulou, et al., Using cool paving materials to improve microclimate of urban areas – design realization and results of the flisvos project, Build. Environ. 53 (14) (2012) 128–136, https://doi.org/10.1016/j.buildenv.2012.01.022.
[51] M. Santamouris, F. Xirafi, N. Gaitani, A. Spanou, M. Saliari, K. Vassilakopoulou, Improving the microclimate in a dense urban area using experimental and theoretical techniques - the case of marousi, athens, Int. J. Vent. 11 (1) (2012) 1–16, https://doi.org/10.1080/14733315.2012.11683966.
[52] A. Synnefa, T. Karlessi, N. Gaitani, M. Santamouris, D.N. Assimakopoulos, C. Papakatsikas, Experimental testing of cool colored thin layer asphalt and estimation of its potential to improve the urban microclimate, Build. Environ. 46 (1) (2011) 38–44, https://doi.org/10.1016/j.buildenv.2010.06.014.
[53] H. Chen, R. Ooka, K. Harayama, S. Kato, X. Li, Study on outdoor thermal environment of apartment block in Shenzhen, China with coupled simulation of convection, radiation and conduction, Energy Build. 36 (12) (2004) 1247–1258, https://doi.org/10.1016/j.enbuild.2003.07.003.
[54] J. Ma, X. Li, Y. Zhu, A simplified method to predict the outdoor thermal environment in residential district, Build. Simul. 5 (2) (2012) 157–167, https://doi.org/10.1007/s12273-012-0079-2.
[55] M.Z. Targhi, S. van Dessel, Potential contribution of urban developments to outdoor thermal comfort conditions: the influence of urban geometry and form in worcester, Massachusetts, USA, Process Eng. 118 (2015) 1153–1161, https://doi.org/10.1016/j.proeng.2015.08.457.
[56] I. Karakounos, A. Dimoudi, S. Zoras, The influence of bioclimatic urban redevelopment on outdoor thermal comfort, Energy Build. 158 (2018) 1266–1274, https://doi.org/10.1016/j.enbuild.2017.11.035.
[57] M. Taleghani, U. Berardi, The effect of pavement characteristics on pedestrians' thermal comfort in Toronto, Urban Clim. 24 (2018) 449–459, https://doi.org/10.1016/j.uclim.2017.05.007.
[58] A. Ghaffarianhoseini, U. Berardi, A. Ghaffarianhoseini, K. Al-Obaidi, Analyzing the thermal comfort conditions of outdoor spaces in a university campus in Kuala Lumpur, Malaysia, Sci. Total Environ. 666 (2019) 1327–1345, https://doi.org/10.1016/j.scitotenv.2019.01.284.
[59] H. Huang, R. Ooka, S. Kato, Urban thermal environment measurements and numerical simulation for an actual complex urban area covering a large district heating and cooling system in summer, Atmos. Environ. 39 (34) (2005) 6362–6375, https://doi.org/10.1016/j.atmosenv.2005.07.018.
[60] H. Lee, H. Mayer, L. Chen, Contribution of trees and grasslands to the mitigation of human heat stress in a residential district of Freiburg, Southwest Germany, Landsc. Urban Plann. 148 (2016) 37–50, https://doi.org/10.1016/j.landurbplan.2015.12.004.
[61] A. Qaid, H. Bin Lamit, D.R. Ossen, R.N. Raja Shahminan, Urban heat island and thermal comfort conditions at micro-climate scale in a tropical planned city, Energy Build. 133 (2016) 577–595, https://doi.org/10.1016/j.enbuild.2016.10.006.
[62] F. Salata, I. Golasi, AdL. Vollaro, RdL. Vollaro, How high albedo and traditional buildings' materials and vegetation affect the quality of urban microclimate. A case study, Energy Build. 99 (2015) 32–49, https://doi.org/10.1016/j.enbuild.2015.04.010.
[63] M. Bruse, H. Fleer, Simulating surface–plant–air interactions inside urban environments with a three dimensional numerical model, Environ. Model. Software 13 (3–4) (1998) 373–384, https://doi.org/10.1016/S1364-8152(98)00042-5.
[64] J. Brozovsky, S. Corio, N. Gaitani, A. Gustavsen, Evaluation of sustainable strategies and design solutions at high-latitude urban settlements to enhance outdoor thermal comfort, Energy Build. 244 (12) (2021) 111037, https://doi.org/10.1016/j.enbuild.2021.111037.
[65] Y. Toparlar, B. Blocken, P.E.J. Vos, G. van Heijst, W.D. Janssen, T. van Hooff, et al., CFD simulation and validation of urban microclimate: a case study for Bergpolder Zuid, Rotterdam. Build Environ. 83 (2015) 79–90, https://doi.org/10.1016/j.buildenv.2014.08.004.
[66] R. Priyadarsini, W.N. Hien, C.K. Wai David, Microclimatic modeling of the urban thermal environment of Singapore to mitigate urban heat island, Sol. Energy 82 (8) (2008) 727–745, https://doi.org/10.1016/j.solener.2008.02.008.
[67] S. Ebrahimabadi, K.L. Nilsson, C. Johansson, The problems of addressing microclimate factors in urban planning of the subarctic regions, Environ. Plann. B 42 (3) (2015) 415–430, https://doi.org/10.1068/b130117p.
[68] W.L. Oberkampf, T.G. Trucano, Verification and validation in computational fluid dynamics, Prog. Aero. Sci. 38 (2002) 209–272.
[69] M. Schatzmann, B. Leitl, Issues with validation of urban flow and dispersion CFD models, J. Wind Eng. Ind. Aerod. 99 (4) (2011) 169–186, https://doi.org/10.1016/j.jweia.2011.01.005.
[70] American Institute of Aeronautics and Astronautics, AIAA Guide for the Verification and Validation of Computational Fluid Dynamics Simulations, American Institute of Aeronautics and Astronautics, Reston, VA, 1998.
[71] N. Antoniou, H. Montazeri, M. Neophytou, B. Blocken, CFD simulation of urban microclimate: validation using high-resolution field measurements, Sci. Total Environ. 695 (2019) 133743, https://doi.org/10.1016/j.scitotenv.2019.133743.
[72] K. Takahashi, H. Yoshida, Y. Tanaka, N. Aotake, F. Wang, Measurement of thermal environment in Kyoto city and its prediction by CFD simulation, Energy Build. 36 (8) (2004) 771–779, https://doi.org/10.1016/j.enbuild.2004.01.033.
[73] W.T.L. Chow, R.L. Pope, C.A. Martin, A.J. Brazel, Observing and modeling the nocturnal park cool island of an arid city: horizontal and vertical impacts, Theor. Appl. Climatol. 103 (1–2) (2011) 197–211, https://doi.org/10.1007/s00704-010-0293-8.
[74] I. Kaoru, K. Akira, K. Akikazu, The 24-h unsteady analysis of air flow and temperature in a real city by high-speed radiation calculation method, Build. Environ. 46 (8) (2011) 1632–1638, https://doi.org/10.1016/j.buildenv.2011.01.029.
[75] X. Yang, L. Zhao, M. Bruse, Q. Meng, Evaluation of a microclimate model for predicting the thermal behavior of different ground surfaces, Build. Environ. 60 (2013) 93–104, https://doi.org/10.1016/j.buildenv.2012.11.008.
[76] K. Maragkogiannis, D. Kolokotsa, E. Maravelakis, A. Konstantaras, Combining terrestrial laser scanning and computational fluid dynamics for the study of the urban thermal environment, Sustain. Cities Soc. 13 (2014) 207–216, https://doi.org/10.1016/j.scs.2013.12.002.
[77] U. Berardi, Y. Wang, The effect of a denser city over the urban microclimate: the case of Toronto, Sustainability 8 (8) (2016) 822, https://doi.org/10.3390/su8080822.
[78] J. Allegrini, J. Carmeliet, Simulations of local heat islands in Zürich with coupled CFD and building energy models, Urban Clim. 24 (2018) 340–359, https://doi.org/10.1016/j.uclim.2017.02.003.
[79] K. Park, Analysis of micro-climate on the programs of urban infrastructure regeneration in J city, Republic of Korea, Urban For. Urban Green. 27 (2017) 43–49.
[80] Y. Toparlar, B. Blocken, B. Maiheu, G.J.F. van Heijst, The effect of an urban park on the microclimate in its vicinity: a case study for Antwerp, Belgium, Int. J. Climatol. 38 (2) (2018) e303–e322, https://doi.org/10.1002/joc.5371.
[81] Y. Toparlar, B. Blocken, B. Maiheu, G. van Heijst, Impact of urban microclimate on summertime building cooling demand: a parametric analysis for Antwerp, Belgium, Appl. Energy 228 (2018) 852–872, https://doi.org/10.1016/j.apenergy.2018.06.110.
[82] J. Brozovsky, S. Corio, N. Gaitani, A. Gustavsen, Microclimate analysis of a university campus in Norway, IOP Conf. Ser. Earth Environ. Sci. 352 (1) (2019), https://doi.org/10.1088/1755-1315/352/1/012015.
[83] Y. Yang, J. Li, Study on urban thermal environmental factors in a water network area based on CFD simulation, Environ. Technol. Innov. 20 (2020) 101086, https://doi.org/10.1016/j.eti.2020.101086.
[84] J. Wieringa, Updating the Davenport roughness classification, J. Wind Eng. Ind. Aerod. 41 (1–3) (1992) 357–368, https://doi.org/10.1016/0167-6105(92)90434-C.
[85] E. Lundstad, O.E. Tveito, Homogenization of Daily Mean Temperature in Norway, 2016.
[86] Meteorologisk Institutt, eKlima: free access to weather- and climate data from Norwegian Meteorological Institute from historical data to real time observations. Normals, Available from: http://sharki.oslo.dnmi.no/portal/page?_pageid=73,39035,73_39049&_dad=portal&_schema=PORTAL.
[87] J.B. Palter, The role of the Gulf Stream in European climate, Ann. Rev. Mar. Sci. 7 (2015) 113–137, https://doi.org/10.1146/annurev-marine-010814-015656.
[88] M. Xu, B. Hong, J. Mi, S. Yan, Outdoor thermal comfort in an urban park during winter in cold regions of China, Sustain. Cities Soc. 43 (2018) 208–220, https://doi.org/10.1016/j.scs.2018.08.034.
[89] W. Liu, Y. Zhang, Q. Deng, The effects of urban microclimate on outdoor thermal sensation and neutral temperature in hot-summer and cold-winter climate, Energy Build. 128 (2016) 190–197, https://doi.org/10.1016/j.enbuild.2016.06.086.

[90] M. Nikolopoulou, S. Lykoudis, Thermal comfort in outdoor urban spaces: analysis across different European countries, Build. Environ. 41 (11) (2006) 1455–1470, https://doi.org/10.1016/j.buildenv.2005.05.031.

[91] B. Yang, T. Olofsson, G. Nair, A. Kabanshi, Outdoor thermal comfort under subarctic climate of north Sweden – a pilot study in Umeå, Sustain. Cities Soc. 28 (2017) 387–397, https://doi.org/10.1016/j.scs.2016.10.011.

[92] J. Strømann-Andersen, P.A. Sattrup, The urban canyon and building energy use: urban density versus daylight and passive solar gains, Energy Build. 43 (8) (2011) 2011–2020, https://doi.org/10.1016/j.enbuild.2011.04.007.

[93] Franke J, Hirsch C, Jensen AG, Krüs HW, Schatzmann M, Westbury PS et al. Recommendations on the use of CFD in wind engineering. Proc. Int. Conf. Urban Wind Engineering and Building Aerodynamics. COST Action C14, Impact of Wind and Storm on City Life Built Environment, von Karman Institute, Sint-Genesius-Rode, Belgium May 5-7 2004.

[94] Y. Tominaga, A. Mochida, R. Yoshie, H. Kataoka, T. Nozu, M. Yoshikawa, et al., AIJ guidelines for practical applications of CFD to pedestrian wind environment around buildings, J. Wind Eng. Ind. Aerod. 96 (10–11) (2008) 1749–1761, https://doi.org/10.1016/j.jweia.2008.02.058.

[95] B. Blocken, T. Stathopoulos, J. Carmeliet, CFD simulation of the atmospheric boundary layer: wall function problems, Atmos. Environ. 41 (2) (2007) 238–252, https://doi.org/10.1016/j.atmosenv.2006.08.019.

[96] B.E. Launder, D.B. Spalding, The numerical computation of turbulent flows, Comput. Methods Appl. Mech. Eng. 3 (2) (1974) 269–289, https://doi.org/10.1016/0045-7825(74)90029-2.

[97] W. Petersen, FerryBox systems: state-of-the-art in Europe and future development, J. Mar. Syst. 140 (2014) 4–12, https://doi.org/10.1016/j.jmarsys.2014.07.003.

[98] M. Santamouris (Ed.), Environmental Design of Urban Buildings: an Integrated Approach, Earthscan, London, 2006.

[99] A. Goris, K.-J. Schneider, A. Albert (Eds.), Bautabellen für Ingenieure: Mit Berechnungshinweisen und Beispielen, nineteenth ed.Neuwied, Köln: Werner, Wolters Kluwer, 2010.

[100] H.G. Jones, Plants and Microclimate: A Quantitative Approach to Environmental Plant Physiology, third ed., Cambridge University Press, Cambridge, 2013.

[101] P.J. Richards, R.P. Hoxey, Appropriate boundary conditions for computational wind engineering models using the k-ε turbulence model, J. Wind Eng. Ind. Aerod. 46 & 47 (1993) 145–153.

[102] J. Wieringa, Roughness-dependent geographical interpolation of surface wind speed averages, Q. J. Roy. Meteorol. Soc. 112 (1986) 867–889.

[103] R.E. Munn, A. Reimer, Turbulence statistics at 30 and 200 feet at Pinawa, Manitoba, Atmos. Environ. 2 (4) (1968) 409–417, https://doi.org/10.1016/0004-6981(68)90010-3.

[105] W.C. Swinbank, Long-wave radiation from clear skies, Q. J. Roy. Meteorol. Soc. 89 (381) (1963) 339–348.

[106] T.-H. Shih, W.W. Liou, A. Shabbir, Z. Yang, J. Zhu, A new k-ε viscosity model for high Reynolds number turbulent flows, Comput. Fluids 24 (3) (1995) 227–238, https://doi.org/10.1016/0045-7930(94)00032-T.

[107] J. Allegrini, J. Carmeliet, Coupled CFD and building energy simulations for studying the impacts of building height topology and buoyancy on local urban microclimates, Urban Climate 21 (2) (2017) 278–305, https://doi.org/10.1016/j.uclim.2017.07.005.

[108] B. Blocken, P. Moonen, T. Stathopoulos, J. Carmeliet, Numerical study on the existence of the venturi effect in passages between perpendicular buildings, J. Eng. Mech. 134 (12) (2008) 1021–1028.

[109] G.K. Ntinas, X. Shen, Y. Wang, G. Zhang, Evaluation of CFD turbulence models for simulating external airflow around varied building roof with wind tunnel experiment, Build. Simul. 11 (1) (2018) 115–123, https://doi.org/10.1007/s12273-017-0369-9.

[110] S.R. Green, Modelling turbulent air flow in stand of widely-spaced trees, Phoenics J. 5 (1992) 294–312.

[111] J. Liu, J. Chen, T.A. Black, M.D. Novak, E-ε modelling of turbulent air flow downwind of a model forest edge, Bound-Layer Meteorol 77 (1) (1996) 21–44.

[112] C. Sanz, A note on k-ε modelling of vegetation canopy air-flows, Bound-Layer Meteorol 108 (2003) 191–197, https://doi.org/10.1023/A:1023066012766.

[113] M.E. Jensen, H.R. Haise, Estimating evapotranspiration from solar radiation, Proceedings of the American Society of Civil Engineers, Journal of the Irrigation and Drainage Division 89 (1963) 15–41.

[114] Y.J. Huang, H. Akbari, H. Taha, A. Rosenfeld, The potential of vegetation in reducing summer cooling loads in residential buildings, J. Clim. Adv. Meteorol. 26 (9) (1987) 1103–1116, https://doi.org/10.1175/1520-0450(1987)026<1103:TPOVIR>2.0.CO;2.

[115] R. Buccolieri, J.-L. Santiago, E. Rivas, B. Sanchez, Review on urban tree modelling in CFD simulations: aerodynamic, deposition and thermal effects, Urban For. Urban Green. 31 (2018) 212–220, https://doi.org/10.1016/j.ufug.2018.03.003.

[116] J. Klingberg, J. Konarska, F. Lindberg, L. Johansson, S. Thorsson, Mapping leaf area of urban greenery using aerial LiDAR and ground-based measurements in Gothenburg, Sweden, Urban For. Urban Green. 26 (2017) 31–40, https://doi.org/10.1016/j.ufug.2017.05.011.

[117] J.L. Monteith, Evaporation and environment, Symp. Soc. Exp. Biol. 19 (1965) 205–234.

[118] H.L. Penman, The physical bases of irrigation control, Report of the 13th International Horticultural Congress 1–13 (1953).

[119] B. Henderson-Sellers, A new formula for latent heat of vaporization of water as a function of temperature, Q. J. Roy. Meteorol. Soc. 110 (1984) 1186–1190.

[120] Food and Agriculture Organisation of the United Nations, Crop evapotranspiration: guidelines for computing crop water requirements. FAO Irrigation and drainage paper 56 [December 10, 2020]; Available from: http://www.fao.org/3/X0490E/x0490e00.htm#Contents.

[121] H. Mayer, P. Höppe, Thermal comfort of man in different urban environments, Theor. Appl. Climatol. 38 (1987) 43–49.

[122] P. Höppe, The physiological equivalent temperature - a universal index for the biometeorological assessment of the thermal environment, Int. J. Biometeorol. 43 (2) (1999) 71–75, https://doi.org/10.1007/s004840050118.

[123] J. Fischereit, K.H. Schlünzen, Evaluation of thermal indices for their applicability in obstacle-resolving meteorology models, Int. J. Biometeorol. 62 (10) (2018) 1887–1900, https://doi.org/10.1007/s00484-018-1591-6.

[124] Verein Deutscher Ingenieure, VDI 3787 Blatt 2 - Environmental Meteorology: Methods for the Human Beiometeorological Evaluation of Climate and Air Quality for Urban and Regional Planning at Regional Level - Part I: Climate, 2008.

[125] E. Walther, Q. Goestchel, The P.E.T. comfort index: questioning the model, Build. Environ. 137 (2) (2018) 1–10, https://doi.org/10.1016/j.buildenv.2018.03.054.

[126] A. Skartveit, J.A. Olseth, A model for the diffuse fraction of hourly global radiation, Sol. Energy 38 (4) (1987) 271–274.

[127] ANSYS Inc, ANSYS Fluent Theory Guide: Release 2020 R1 January 2020, 2020. Canonsburg, PA.

[128] ANSYS Inc, Fluent User's Guide: Release 2020 R1 January 2020, 2020. Canonsburg, PA.

[129] J.P. van Doormaal, G.D. Raithby, Enhancements of the SIMPLE method for predicting incompressible fluid flows, Numer. Heat Tran. 7 (2) (1984) 147–163, https://doi.org/10.1080/01495728408961817.

[130] K.B. Rajasekarababu, G. Vinayagamurthy, S. Selvi Rajan, Experimental and computational investigation of outdoor wind flow around a setback building, Build. Simul. 12 (5) (2019) 891–904, https://doi.org/10.1007/s12273-019-0514-8.

[131] A. Ricci, I. Kalkman, B. Blocken, M. Burlando, A. Freda, M.P. Repetto, Local-scale forcing effects on wind flows in an urban environment: impact of geometrical simplifications, J. Wind Eng. Ind. Aerod. 170 (2017) 238–255, https://doi.org/10.1016/j.jweia.2017.08.001.

[132] J. Franke, A. Hellsten, H. Schlünzen, B. Carissimo (Eds.), Best Practice Guideline for the CFD Simulation of Flows in Th Urban Environment: COST Action 732 Quality Assurance and Improvement of Microscale Meteorological Models, Univ. of Hamburg Meteorological Inst, Hamburg, 2007.

[133] J. Allegrini, V. Dorer, J. Carmeliet, Influence of morphologies on the microclimate in urban neighbourhoods, J. Wind Eng. Ind. Aerod. 144 (2015) 108–117, https://doi.org/10.1016/j.jweia.2015.03.024.